STAR Analysis Note: Measurement of transverse polarization of Λ in unpolarized pp collision at 200GeV

Taoya Gao, Qinghua Xu, Yi Yu, and Jinlong Zhang

August 20, 2025

Contents

List of Figures

List of Tables

1 Dataset

The data set (summarized in Table 1.1) used in this analysis includes pp200long_2015, pp200long2_2015 and pp200trans_2015 at present, which were taken in RHIC-STAR at $\sqrt{s} = 200$ GeV in pp collision with 689, 557 and 686 good physics runs respectively. The sum of the integrated luminosity of the three samples is about 133 pb^{-1}. Jet-Patch triggers(JP1, JP2), as shown in Table.1.2, are used in the analysis.

System and energy	**pp collisions at $\sqrt{s} = 200$ GeV**		
Data	pp200long_2015	pp200trans_2015	pp200long2_2015
Number of run	689	686	557
Total events	436 M	862 M	728 M
Luminosity(pb^{-1})	29	52	52
Production	P16id		
Trigger	JP1(470404, 480404, 480414, 490404) JP2(470401, 480401, 480411, 490401)		

Table 1.1: Dataset in this analysis.

Trigger	ID	Threshold (ADC channels)	Equivalent E_T (GeV)
JP1	490404	28	5.4
JP2	490401	36	7.3

Table 1.2: Triggers used in the analysis

Some sub-detectors of STAR such as the TPC, BEMC, and EEMC are used in this analysis. The Events with primary vertex z within ±90 cm from the center of TPC along the beam direction are selected. The primary vertex rank must be larger than $10e6$, with about 5.93×10^8 events after z cuts. Fig. 1.1 showed the primary vertex z distribution before the selection of primary vertex z.

2 $\Lambda/\overline{\Lambda}$ reconstruction

The Λ hyperon characterized by self-analyzing weak decay has played a special role in the field of spin physics [1]. The $\Lambda(\overline{\Lambda})$ candidates are reconstructed via the weak decay channel: $\Lambda \to p+\pi^-$ ($\overline{\Lambda} \to \overline{p}+\pi^+$), following a similar procedure as in Ref. [2] except that the Time of Flight (TOF) hit matching is not required for the pion track. Firstly, good-quality tracks are obtained by following criteria:

- Track flag: $0 \sim 1000$

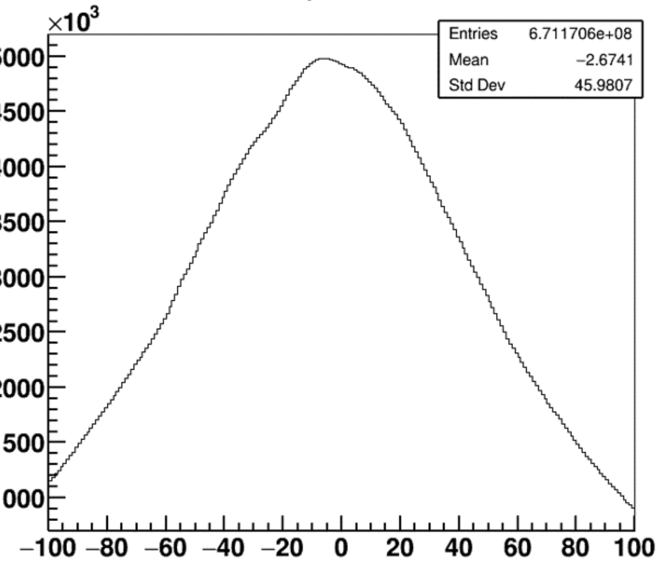

Figure 1.1: distribution of the primary vertex z.

- p_T :$>$ 0.15 GeV
- NHits > 15
- NHits/NHitsPoss > 0.52
- DCA $<$ 30cm

The TPC detector provides charge tracking and particle identification, which is used to select protons and π from a bunch of particles by ionization energy loss dE/dx. Because of the limited resolution of TPC detector, the capability of particle identification is reduced for charge particles with large momentum that are shown in Fig.2.1 (a) [3] that present ionization energy loss of four type particles, $e^{\pm}$, $p\,(\bar{p})$, $\pi^{\pm}$ and $K^{\pm}$. The $n\sigma$ cut of proton candidate, for example, was required to be within $\pm 3\sigma$ to the theoretical values of dE/dx for proton. This cut is a reasonable value to balance the statistics and particle identification quality. Two daughter tracks with opposite charges are paired and hyperon p_T-dependent topological selection criteria, summarized in Tab. 2.1 and 2.2, are applied to suppress the background with an acceptable percentage of about 10%. Figure 2.2 shows the invariant mass distribution of Λ.

3 V_0 jet reconstruction

In order to implement the measurement of Λ polarization contribution from the fragmentation process, we need to reconstruct jet. The momentum direction of jet will be regarded as the direction of the fragmenting parton. This is also critical to determine the polarization direction of Λ. In this analysis, the jet was reconstructed with anti-k_T algorithm with following parameter sets.

- Reconstruction: anti-k_T with $R = 0.6$
- Tracks: primary track with $p_T > 0.2$ GeV and DCA < 3 cm
- Towers are required to have $E_T > 0.2$ GeV

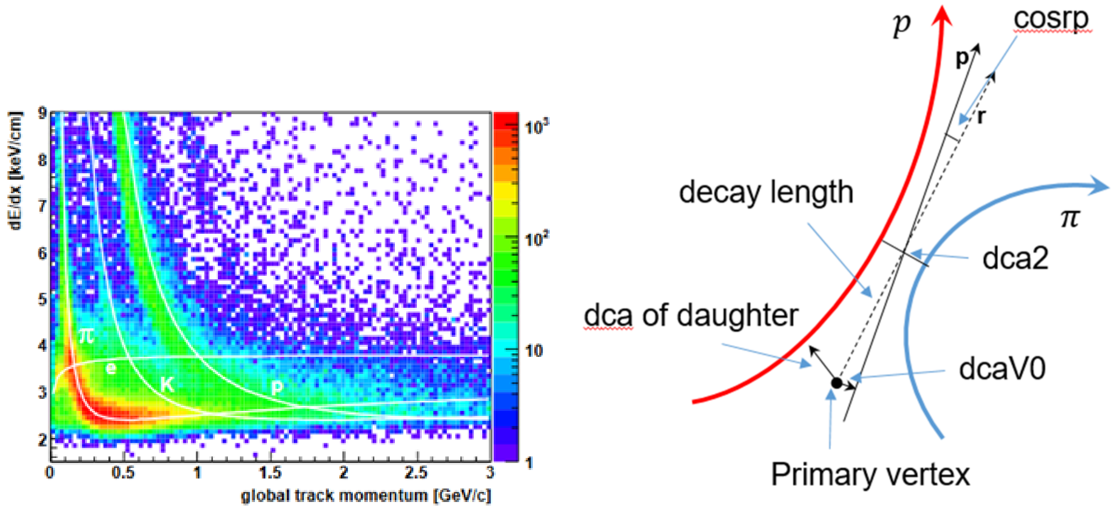

(a) dE/dX distribution of TPC (b) Λ reconstruction

Figure 2.1: (Left) particle identification of TPC by dE/dx, (Right) the schematic of Λ reconstruction.

$\Lambda(\overline{\Lambda})$ topological cuts							
p_T [GeV/c]	$0-1$	$1-2$	$2-3$	$3-4$	$4-5$	$5-6$	>6
$\lvert n\sigma\rvert <$	1.5	1.5	1	1	1	1	1
$DCA2(cm) <$	0.65	0.65	0.60	0.55	0.50	0.45	0.40
$DCA_p(cm) >$	0.45	0.35	0.30	0.15	0.005	0.005	0.005
$DCA_\pi(cm) >$	0.65	0.65	0.60	0.55	0.50	0.50	0.50
$DCAV0(cm) <$	0.55	0.65	0.75	1.0	1.0	1.0	1.0
$DecayLength(cm) >$	3.0	3.0	3.5	3.5	4.0	4.5	4.5
$cosrp >$	0.995	0.995	0.995	0.995	0.995	0.995	0.995

Table 2.1: The table of $\Lambda(\overline{\Lambda})$ topological cuts at different p_T ranges

K_s^0 topological cuts							
p_T [GeV/c]	$0-1$	$1-2$	$2-3$	$3-4$	$4-5$	$5-6$	>6
$\lvert n\sigma\rvert <$	1.35	1.35	1.35	1.40	1.45	1.50	1.70
$DCA2(cm) <$	0.65	0.65	0.65	0.55	0.55	0.50	0.35
$DCA_p(cm) >$	0.60	0.55	0.50	0.35	0.30	0.25	0.20
$DCA_\pi(cm) >$	0.60	0.55	0.50	0.35	0.30	0.25	0.20
$DCAV0(cm) <$	0.65	0.70	0.80	0.90	0.90	0.90	0.90
$DecayLength(cm) >$	3.55	3.60	3.70	3.75	3.80	4.0	5.5
$cosrp >$	0.995	0.995	0.995	0.995	0.995	0.995	0.995

Table 2.2: The table of K_s^0 topological cuts at different p_T ranges

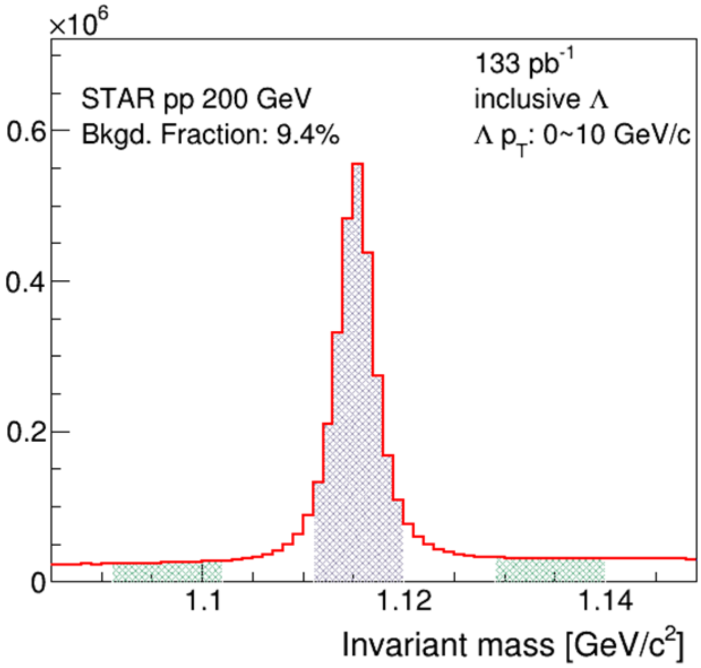

Figure 2.2: The invariant mass distribution of reconstructed Λ .

- The jet $p_T > 5$ GeV
- Anti-proton energy correction

The final production of the whole fragmentation process consists of a variety of charge particles and neutral particles. We aim to probe the Λ polarization in final states. Therefore, the jets used here is full-jet consisting of both charge tracks from TPC and neutral energy from EEMC and BEMC. Only primary tracks with DCA $< 3cm$ are utilized for jet reconstruction. To reduce noise background, the track p_T and tower energy E_T are required to be larger than 0.2 GeV. In case of the additional energy deposits in detector from possible annihilation effects of $\bar{p}$ with proton from material of BEMC and EEMC, the $\bar{p}$ annihilation correction is necessary(see Section 3.2). Besides, to reduce the other effects from underlying events (UE), we applied off-axis method to do the UE corrections, which helps to reduce the pile-up events. The jet candidates satisfying follow selection cuts are considered in this analysis.

- Jet p_T - UE $p_T > 5$ GeV and pass trigger threshold
- Neutral fraction $R < 0.95$
- Jet η: $-1 < \eta < 1$
- Jet detector η_{det}: $-0.7 < \eta_{det} < 0.9$

The goal of neutral fraction $R < 0.95$ requirements is to avoid the contribution from charge tracks of TPC is too low. The difference between jet η and detector η_{det} is that η_{det} indicates the pseudorapidity of tower position in EMC relative to the TPC center.

3.1 Modification of jet reconstruction

Unlike traditional jet reconstruction in STAR, in this analysis, the reconstructed $\Lambda/\overline{\Lambda}$ candidates will also be added to the input list for jet reconstruction. Meanwhile, the primary tracks associated with the $\Lambda/\overline{\Lambda}$ daughter tracks will be excluded to avoid double counting. The diagram of this process is presented in Fig. 3.1. In some cases, $\Lambda/\overline{\Lambda}$ and K_S^0 may share the same daughter track due to the misidentification between protons and pions. This effect will introduce potential double counting if $\Lambda/\overline{\Lambda}$ and K_S^0 are both added to the same input list for jet reconstruction. To avoid such double counting, the $\Lambda/\overline{\Lambda}$-jets and K_s^0-jets were reconstructed separately.

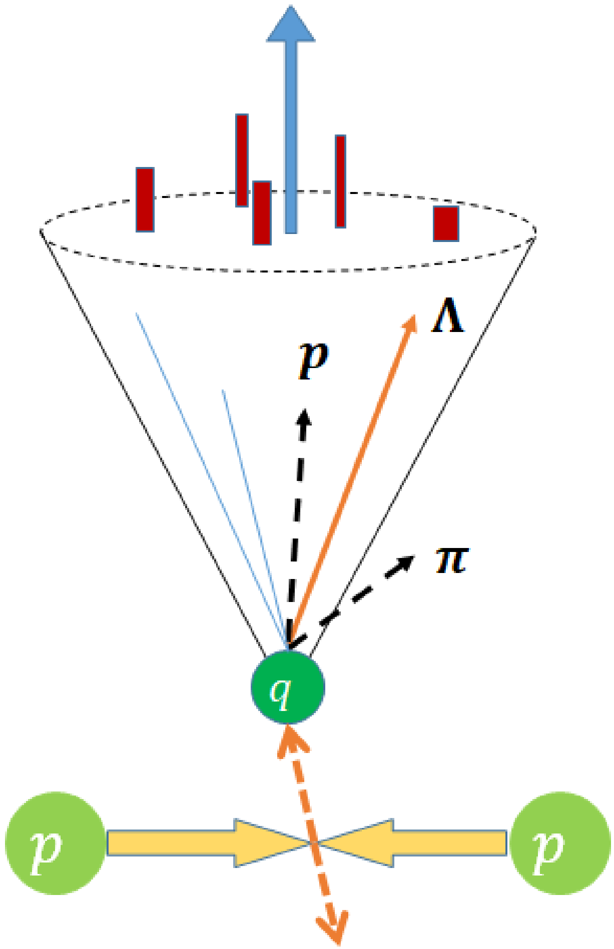

Figure 3.1: The Λ jet reconstruction process, where dashed black lines inside cone denote daughter tracks: p, π that will be excluded from particle list. The red rectangle means tower energy deposited in BEMC or EEMC. The big blue arrow indicates the reconstructed jet direction.

3.2 Anti-proton annihilation correction

The annihilation effects of antiproton produced in the final state with materials of BEMC/EEMC are non-negligible. For example, the $\bar{p}$ decayed from $\bar{\Lambda}$, especially for low momentum, would likely annihilate with protons from BEMC/EEMC materials and deposit additional energy in BEMC/EEMC. This additional energy will also impact the neutral fraction in the process of jet reconstruction and increase the original actual jet energy. Fig.3.2 displays the tower energy distribution deposited in BEMC and EEMC that match to p and $\bar{p}$. According to parity conservation, the behaviors of p and $\bar{p}$ should be similar, which are different from the results in the plots. There is an apparent enhancement at large tower energy for $\bar{p}$. And the mean value of proton tower energy is 0.6 GeV, even only about half of that for $\bar{p}$.

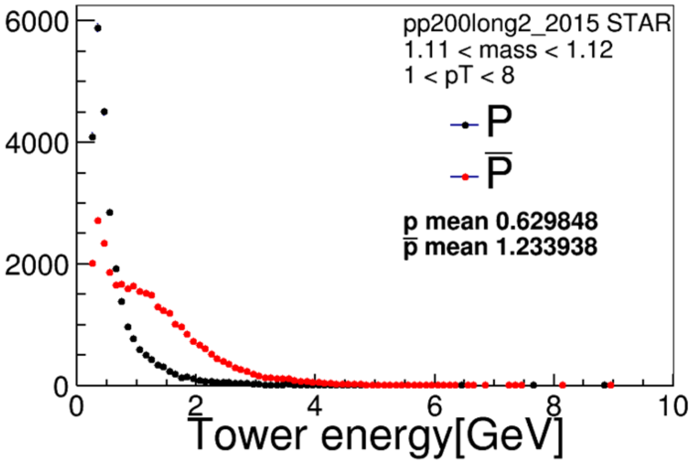

Figure 3.2: Comparison of tower energy of p and $\bar{p}$ matched to BEMC or EEMC.

Nevertheless, the deposited energy of $\bar{p}$ was still less than the theoretical value (twice of proton mass), if annihilated with other detector protons. One of the reasons we suppose might be that the additional energy extended to surrounding towers, which caused the tower energy matched to $\bar{p}$ shift to the low energy range. To include annihilation energy of $\bar{p}$ deposited in calorimeters as much as possible, the tower region matched to charge particle expands from one tower to surrounding 9 towers. As shown in Fig.3.3, the number denotes the tower index in detectors within the phase space constructed by η and ϕ axis.

Significantly, the energy distribution including 9 towers matched to $\bar{p}$ shifts to the large value range with a peak at about 2 GeV. At the same time, No significant changes were observed for p. Such results demonstrate that the annihilation effects of $\bar{p}$ can not be ignored and it is necessary to make corrections. In this analysis, 3×3 towers energy with it central tower matched to $\bar{p}$ are removed from the jet reconstruction.

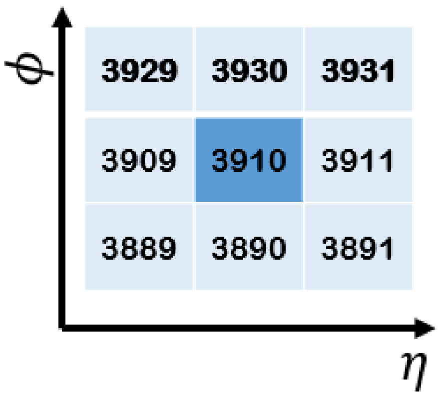

Figure 3.3: Tower map of BEMC that p and $\bar{p}$ matched.

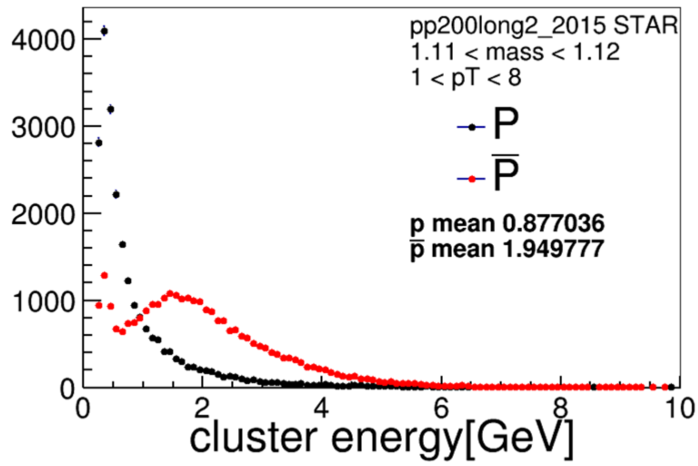

Figure 3.4: Comparison of 3×3 tower energy of p and $\bar{p}$ matched to BEMC or EEMC.

3.3 Underlying events correction

The typical method, off-axis cone[4], was used in this analysis to subtract contributions from underlying events (UE), which contribute mostly low p_T tracks. They are corresponding to all particles produced directly from pile-up or hard scattering of partons, which are regarded as the contamination of jet. The two cones with the same η as jet, but perpendicular to the jet cone, are adopted to evaluate the UE particle yield. As shown in Fig. 3.5, the UE cones, dashed circular line with the radius equal to the jet resolution parameter ($R = 0.6$), are offset by an azimuthal angle $\phi = \pi/2$ with respect to the jet axis.

A general strategy for the UE contamination correction is to subtract the UE contribution to the jet p_T jet-by-jet. The p_T spectra of all particles inside these two UE cone are accumulated and divided by cone area, namely $2\pi R^2$, to obtain the UE p_T density ρ. Hence, the average UE p_T could be obtained through $\rho \times A_{jet}$, where A_{jet} is the area of the jets calculated by the Fastjet package[5].

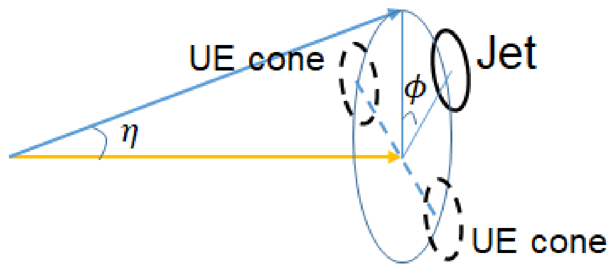

Figure 3.5: Diagram of Off-axis method.

However, in the multi-jet events, two or more jets with the same η but the $\Delta\phi = \pi/2$ probably occurred in the same event. It means the UE contribution to the jet p_T would be significantly overestimated, which will enhance the UE p_T. Figure 3.6 shows the UE p_T spectra with jet number dependence, and the average UE p_T increases with jet numbers. As a result, the jet p_T will be over corrected, if using these raw UE p_T that was enhanced by contribution from a real jet. What we did for this issue is to modify the UE region selection by including a protection that when a jet was found nearby UE cones ($\Delta R \leq 1.2$), particles in that UE cones will be excluded from the UE p_T calculations.

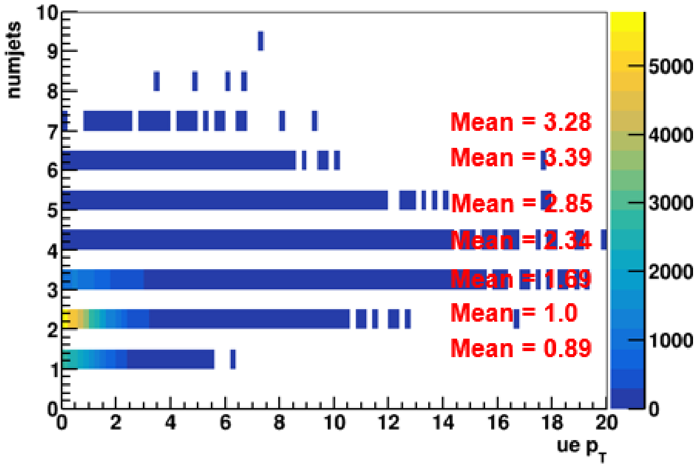

Figure 3.6: Underlying events p_T and average UE p_T versus number of jets.

The threshold of the jet that was regarded as a jet found nearby UE cones is set as 4 GeV. Following plots, Fig. 3.7, show the UE results after applying a protection mechanism in two UE cones. Apparently, this protection mechanism impacts largely on the UE p_T calculations, especially for multi-jets events. On the other hand, the threshold setup of a jet is also a crucial factor. Lower threshold means a jet would be identified as a real jet easier. See for the two plots of Fig. 3.7, the different minimum jet p_T are 4 GeV and 2.5 GeV respectively and resulted in different average UE p_T. In the left plot, the label '3coneUE' denotes another cone at opposite azimuth relative to the jet was regarded as UE cone either, which aimed to compensate the deficiency of UE cone resulted by protection mechanism but was canceled at final analysis. To keep things consistent, all parameters of jet nearby UE cones are the same as jet parameters above.

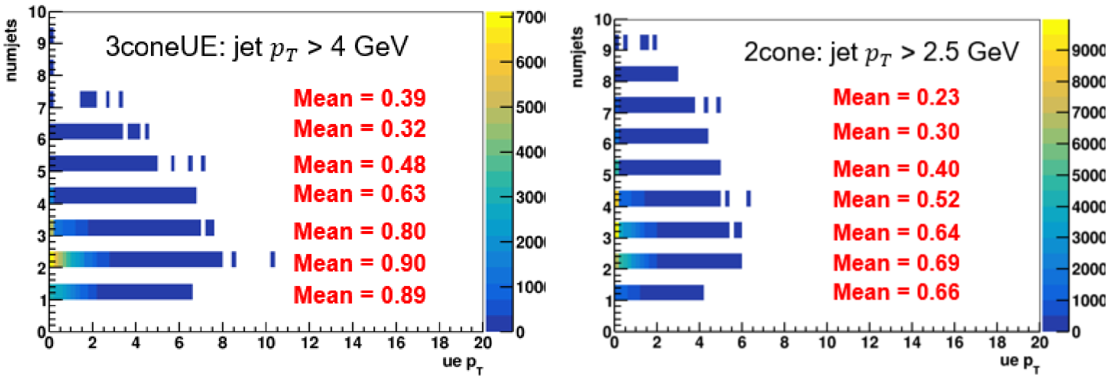

Figure 3.7: Underlying events p_T and average UE p_T versus number of jets.

4 MC Simulation

To correct acceptance effects from limited detector acceptance range and efficiency, we need to obtain acceptance functions corresponding to the STAR detector, which could be available by Monte Carlo (MC) simulation. There are many MC generators for the simulation of the pp collisions. In this analysis, simulation events are generated by PYTHIA6.4.28 [6] and then run through GEANT3 [7] based on STAR detectors.

4.1 Parameters set

The simulated events should be embedded into "zero-bias" data which was taken by triggered randomly in the period of run. Because these events with zero-bias trigger could be used to simulate beam background and pile-up events to make the simulation closer to the actual conditions. However, based on our study, we find it does not greatly affect the acceptance function without zero-bias data from simulation. The simulation setup are listed following:

- PYTHIA6.4.28 + GEANT3
- ptHard > 4 GeV
- Energy 200 GeV
- Geometry: y2015c
- $\Lambda/\overline{\Lambda}$ filter: promise every event include at least one $\Lambda/\overline{\Lambda}$ with $p_T > 0.5$ GeV
- Primary vertex: Gaussian distributions with $\sigma_x = 0.026$ cm, $\sigma_y = 0.015$ cm,$\sigma_z = 41.48$ cm

The reason why ptHard is larger than 4 GeV, rather than the usual several separate regions from 2 to 35, is to increase simulation efficiency with jet-patch trigger as much as possible while suppress edge effects of trigger threshold as low as possible, simultaneously. Figure 4.1 shows the ratio of contributions of different ptHard ranges to jet p_T spectra. The left plot is for the JP1 trigger and the right one is for the JP2 trigger. The percentage of the contribution to jet p_T spectrum from ptHard $2 \sim 3$ GeV is about 5.68% and from ptHard $3 \sim 5$ GeV is about 7.53%. Moreover, the efficiency for a event from ptHard $2 \sim 4$ GeV that passes trigger threshold is too low to obtain sufficient statistics within acceptable time duration. Therefore, 4 GeV is an appropriate value for minimum ptHard.

The goal of applying $\Lambda/\overline{\Lambda}$ filter is to increase simulation efficiency and save disk space by selecting events that include at least one Λ or $\bar{\Lambda}$ with $p_T > 0.5$ GeV. For the JP1 and JP2 triggers, we also applied the trigger simulator to simulate the trigger response. The same algorithms as the data are applied in MC simulation to reconstruct $\Lambda/\overline{\Lambda}$ and jet.

4.2 Particle identification correction

In the analysis, we encountered a severe issue with the MC sample: the central value of $n\sigma$ distribution from the MC sample significantly deviated from its theoretical value and also differed from the real data distribution. The distributions of $n\sigma$ for protons in both the MC and real data samples are shown below in Fig.4.2. The center of the proton $n\sigma$ distribution in the MC sample is shifted towards negative values by approximately one sigma. In contrast, the center of the proton $n\sigma$ distribution in the data sample is consistent with zero. This issue will introduce potential biases to the measurements as same nσ selection cuts were applied to both read data and MC samples.

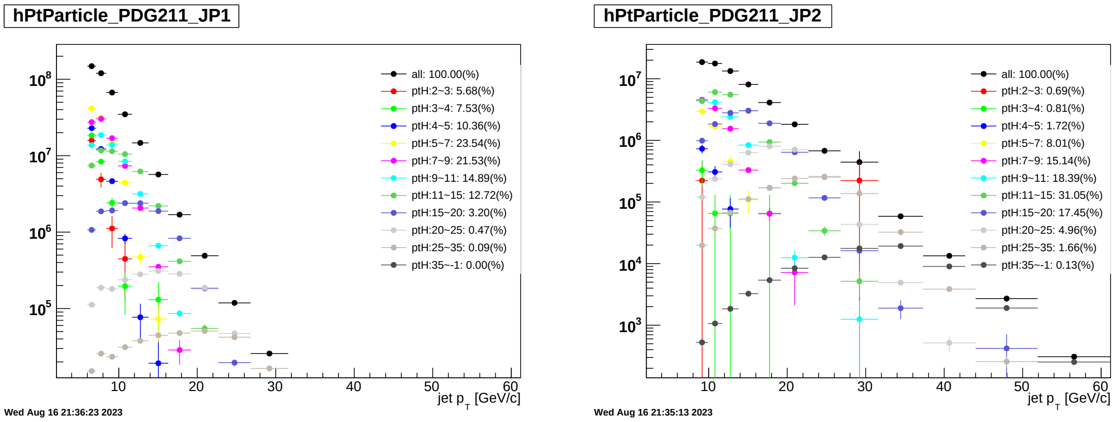

Figure 4.1: Jet contributions from different ptHard ranges.

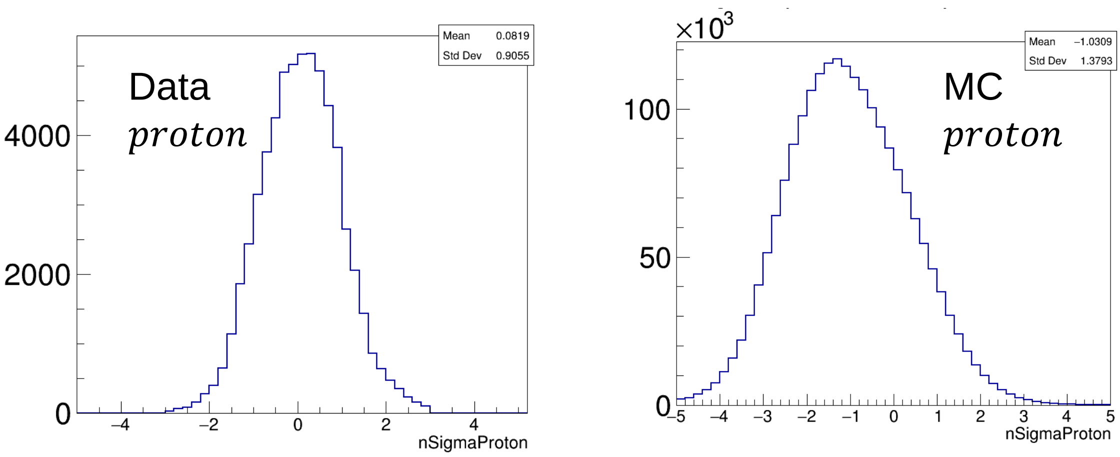

Figure 4.2: $n\sigma$ distributions of proton in data and MC sample

Upon careful examination, we found that the cause of this phenomenon is due to inadequate simulation of particle ionization energy loss in the gas during the generation of the MC sample. The blue and green lines in the Fig. 4.3 below represent the fits to the ionization energy loss as a function of momentum for protons at the detector level and association level in the MC sample, respectively. These do not match the distribution of ionization energy loss versus momentum for protons in the real data sample. Similar issues are observed for other types of particles as well.

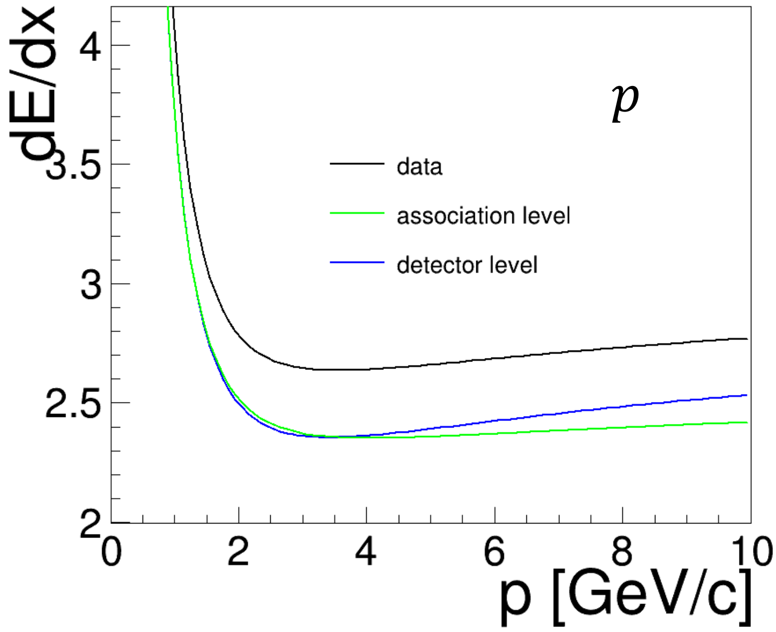

Figure 4.3: dE/dx vs momentum distributions of proton in data and MC sample

To avoid the bias introduced by suboptimal simulation of ionization energy loss, we must apply a correction. The method involves fitting the distribution of the $n\sigma$ mean values as a function of momentum to ascertain the deviation from the theoretical curve. For this step, we require a clean sample of particles, so we extracted particles at the association level, which are associated directly with pure particles produced by PYTHIA. The left plot of Fig.4.4 shows a 2-dimensional distribution of proton $n\sigma$ as a function of momentum. And right plot is the distribution of the mean value of $n\sigma_p$ versus proton momentum, which shows a complex dependence. Then, we subtract the corresponding deviation value from each particle's $n\sigma$, realigning it with the theoretical value.

4.3 Comparison of pure MC and data

The reconstruction of Λ, $\overline{\Lambda}$, and K_s^0 in both MC and data employed identical reconstruction methods, selection criteria, and topological cuts to ensure consistency. Comparisons of the data and MC simulation are shown in the Appendices. We can find a good agreement for p_T between the data and MC simulation.

For pseudo-rapidity η and azimuth angle ϕ, some sectors of TPC issued this year resulted in the nonuniform distributions of azimuth angle ϕ and asymmetrical η distribution relative to zero. However, MC simulation is not consistent with data, which means GEANT3 based on

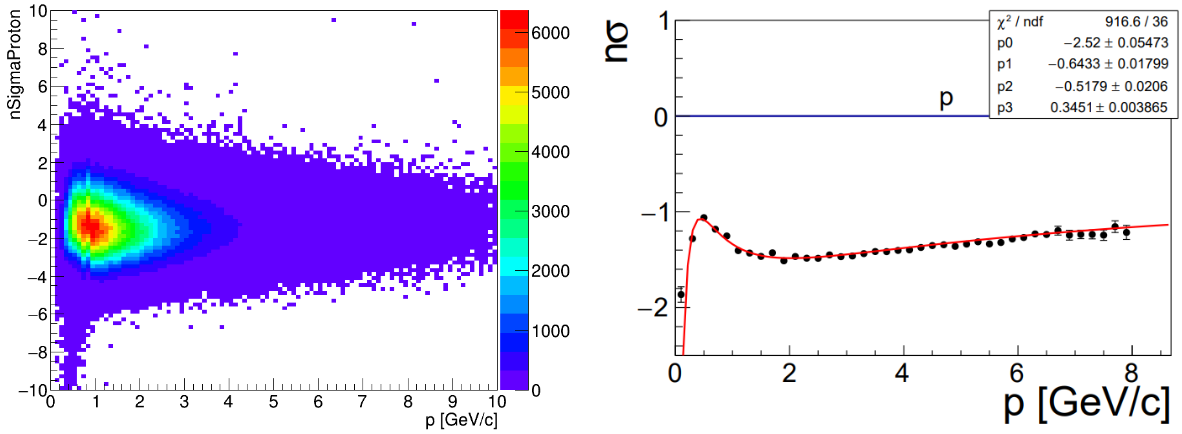

Figure 4.4: Left: 2-dimensional distribution of proton $n\sigma$ as a function of momentum ; Right: the mean value of $n\sigma_p$ versus proton momentum

the STAR detector did not simulate perfectly the true status of the STAR detector. These will influence acceptance correction. Simultaneously, the statistic of the MC simulation sample is highly hard to produce due to low efficiency and limited resources. We just utilize it to check the new method of acceptance correction and estimate trigger bias.

5 Mixed Events

The biggest disadvantage of MC simulation is its statistics are still not enough for acceptance correction of data, which resulted statistical uncertainty of results are too large to obtain a definite conclusion. Thus, another alternative method, named mixed-event method[8], is proposed for this analysis. This is a popular method utilized widely to estimate combination backgrounds by mixing different tracks from randomly different events, the details can be found in reference [8]. An important reason we want to use the mixed event method is its fast production and smaller storage space, which could save lots of time and computer resources.

In this analysis, the mixed method is a little different but with the same principle. A reconstructed Λ particle will be embedded into a different event to form a mixed event, then using this event to reconstruct Λ jet. The procedures are shown in Fig.5.1. Of course, these two events must be required with the same trigger and their discrepancy of primary vertex z is smaller than 5 centimeters, and mixed events must be applied to the individual run aiming to ensure similar conditions as much as possible. Owing to there being no correlation between Λ and jet from different events, no physic signal of polarization will be obtained theoretically, and the original correlation between Λ and jet at the SE is also broken simultaneously.

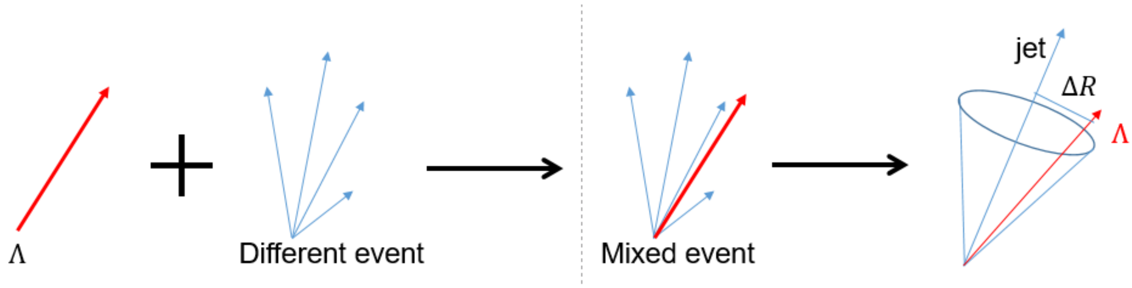

Figure 5.1: Mixed event procedure

5.1 The research of Mixed-event methods

There are two types of mixed events in this analysis based on constraints of Λ and jet in different events. For example, at one event, the azimuth phase space is separated into two sections, the jet areas and off-axis regions, as shown in Fig.5.2. The Fig. 5.3 shows near-jet mixed events and corresponding comparison of ΔR distribution. If there are no constraints between Λ and jet at mixed event, the Λ will located randomly at any region that was described above that named as random mixed events. Therefore, it is possible for Λ to reconstruct a fake jet when it located at off-axis regions where none jet exist. It means this jet was dominated by Λ particle, which was verified in Fig. 5.4. This condition might affect jet p_T distribution and acceptance correction. The Fig. 5.4 shows mixed events when Λ located at off-axis regions, likely to underlying event (UE) cone. The ΔR distribution is inconsistent with the same event.

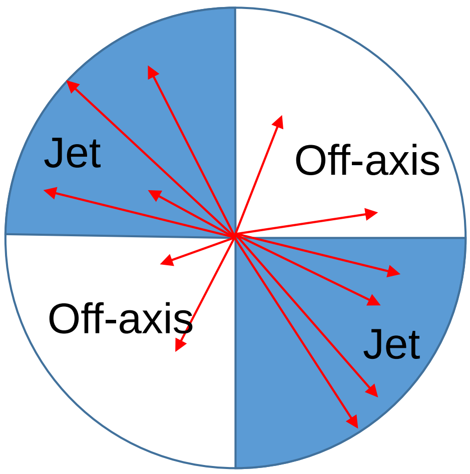

Figure 5.2: Azimuth phase space

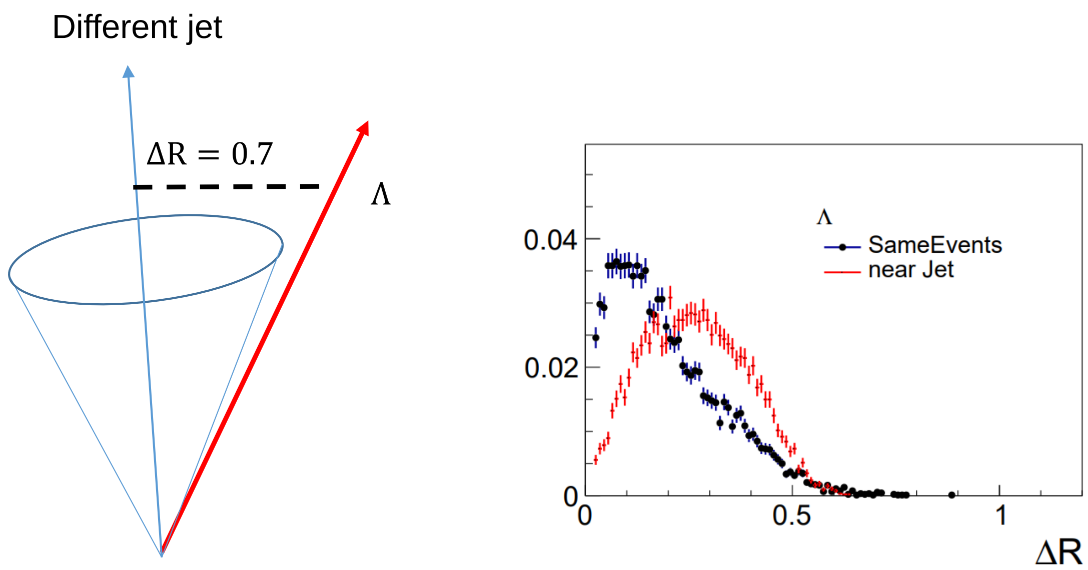

Figure 5.3: The near-jet mixed events

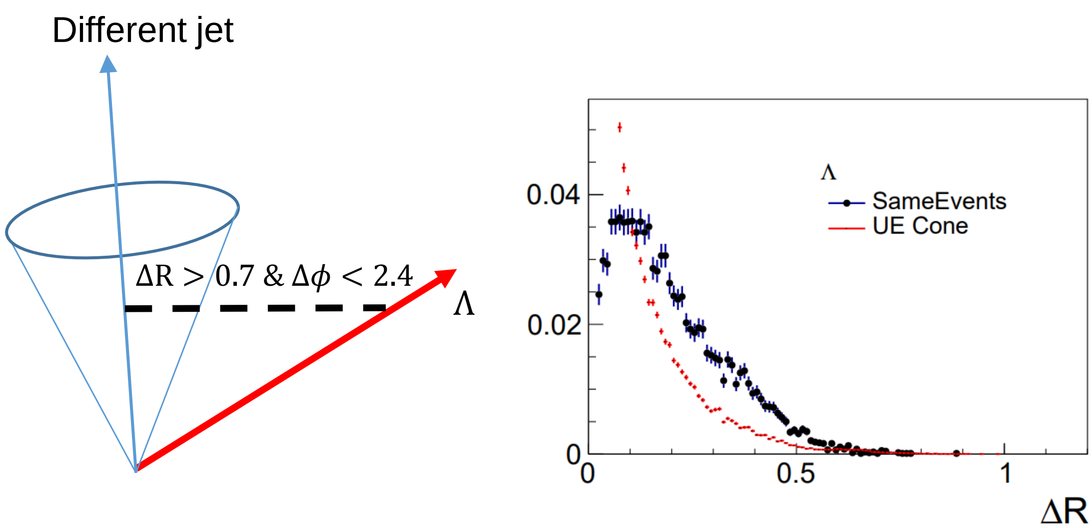

Figure 5.4: The off-jet mixed events

To assess the magnitude of the influence, Λ was required to be near the jet with $\Delta R < 0.7$ in mixed events prior to jet reconstruction. The quality comparison between random mixed events and near-jet mixed events is illustrated in the following figures. There is no significant difference in the jet p_T distribution, with the exception of the low p_T range. Removing mixed events from the off-axis region would significantly reduce the number of fake jets with low p_T that are predominantly composed of Λ particle. A positive outcome is that near-jet mixed events have improved the consistency of the z distribution with SE. Nevertheless, j_T distribution has not seen substantial improvement, and inconsistency persists.

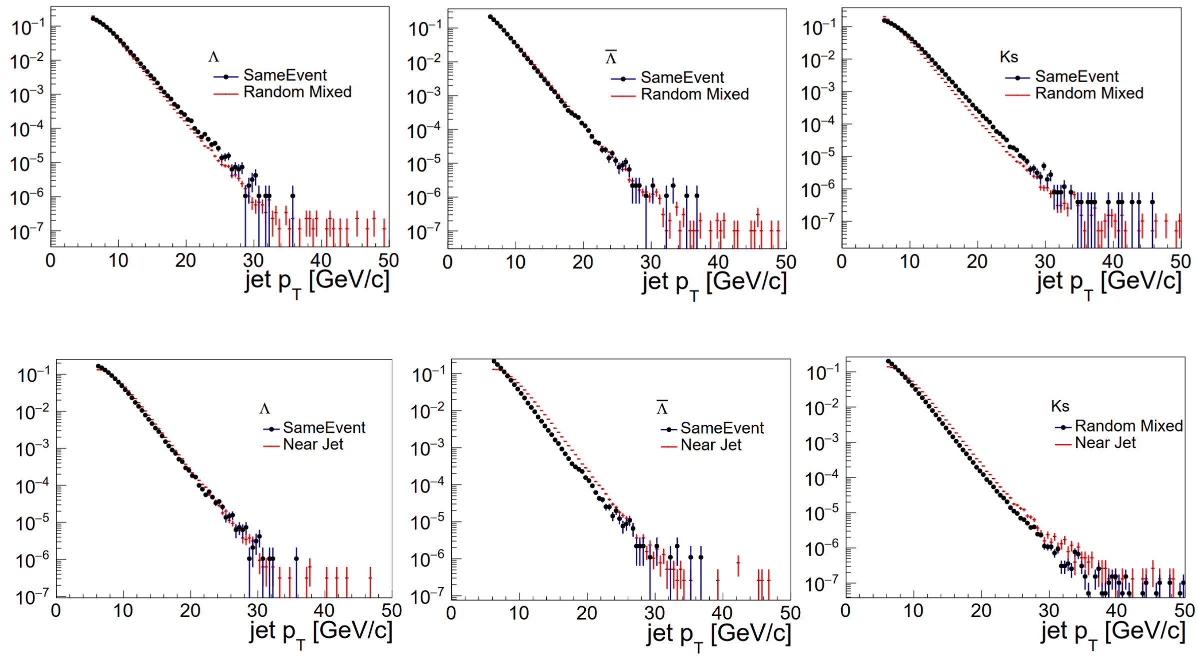

Figure 5.5: Top panel: comparisons of jet p_T between SE and random ME; Bottom panel: comparisons of jet p_T between SE and near-jet ME

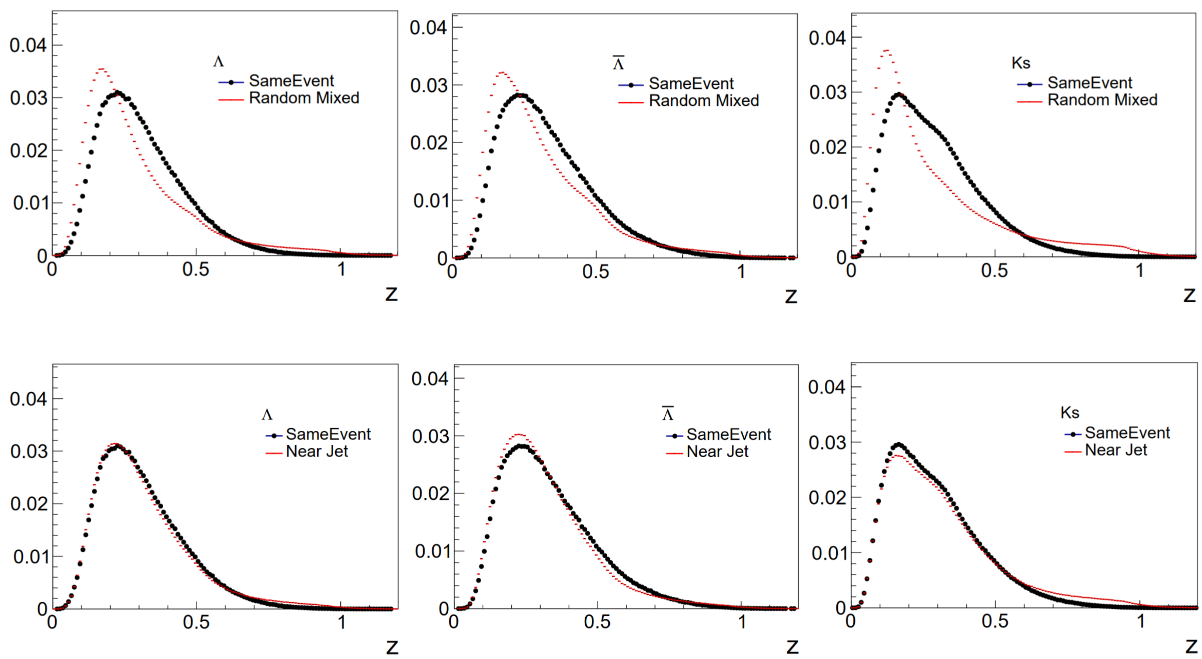

Figure 5.6: Top panel: comparisons of z between SE and random ME; Bottom panel: comparisons of z between SE and near-jet ME

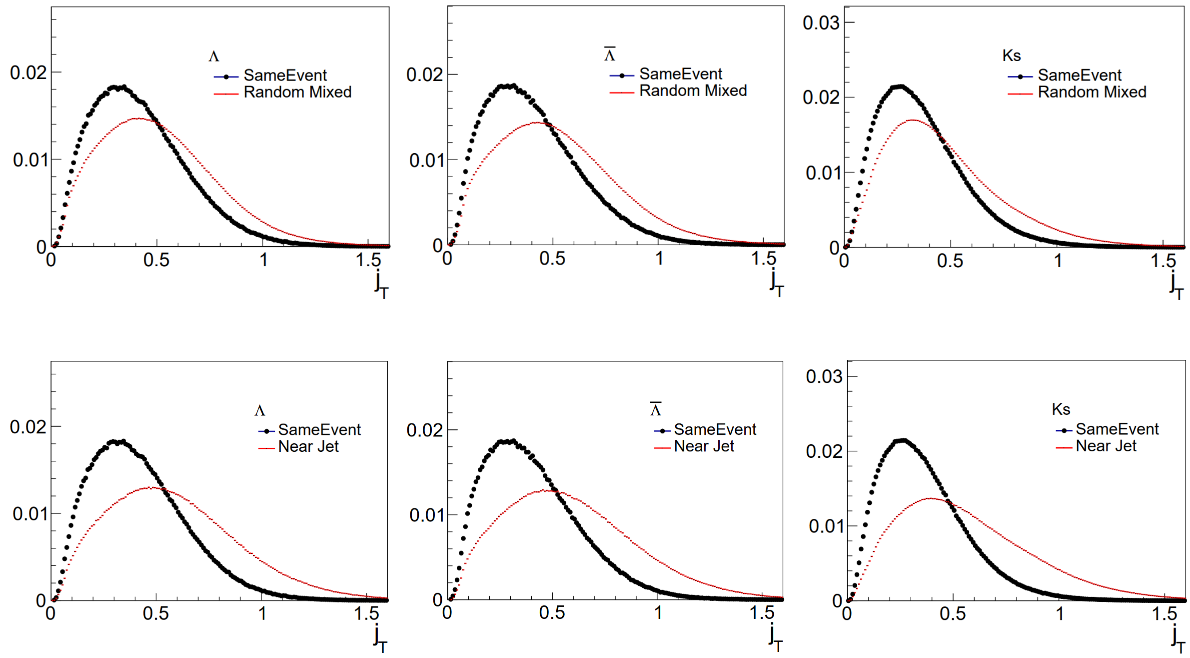

Figure 5.7: Top panel: comparisons of j_T between SE and random ME; Bottom panel: comparisons of j_T between SE and near-jet ME

We also compared Λ and $\overline{\Lambda}$ $\cos\theta^*$ distributions of mixed events generated by the different methods. The consistency of their distributions was very good, indicating that the off-axis region has a minor impact on the correction of the acceptance. However, the near-jet mixed events were closer to the true events, so we still used this method for acceptance correction in this analysis.

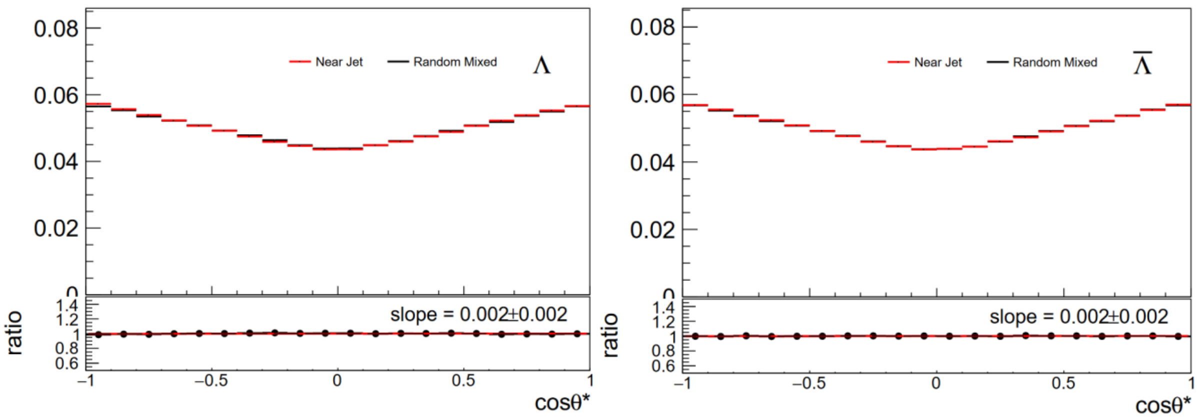

Figure 5.8: Comparison of $\cos\theta^*$ between random and near-jet mixed event

5.2 Closure test in MC

The closure test for this method is essential to determine whether the mixed-event technique can be effectively applied for acceptance correction in this analysis. The following investigation of mixed events is based on unpolarized Monte Carlo (MC) samples, generated using Pythia 6 and GEANT3, as previously mentioned. First, we must verify whether the mixed-event method introduces any non-physical spurious signals.

We have generated a mixed-event sample using MC simulation data, applying the same jet reconstruction algorithm and selection criteria as in the original analysis. Since Λ hyperons in mixed events do not originate from the same hard scattering process as the jets, the Λ-jet correlation in mixed events is expected to differ from that in same events. Figure 5.11 compares the distributions of key observable ΔR, which characterize the Λ-jet correlation between mixed and same events.

- ΔR represents the angular separation between the Λ hyperon and the jet axis in the η-ϕ plane.

$$\Delta R = \sqrt{(\Delta\eta)^2 + (\Delta\phi)^2} \tag{5.1}$$

To improve the consistency of correlations quantities between the mixed and the same events, we implement a reweighting procedure to match the ΔR distribution between data and mixed events. However, a purely one-dimensional ΔR reweighting fails to capture important angular correlations, particularly the distinct η and ϕ-dependence of Λ-jet correlations. This is especially critical for the $\Delta\eta$ distribution, which exhibits significant pseudorapidity dependence due to detector acceptance effects. As illustrated in Figure 5.9 and Figure 5.10, the two-dimensional distributions of ($\Delta\eta$, $\Delta\phi$) versus jet η reveal complex correlation patterns that cannot be reproduced by ΔR alone. These distributions show:

- $\Delta\eta$ broadening at high $|\eta|$
- Edge effects near detector acceptance boundaries

To properly account for these effects, we implement a three-dimensional reweighting scheme based on:

$$\left(\Delta\eta, \Delta\phi, \eta^{\text{jet}}\right) \tag{5.2}$$

This comprehensive approach ensures proper descriaption of:

- The full angular correlation structure
- η-dependent detector effects

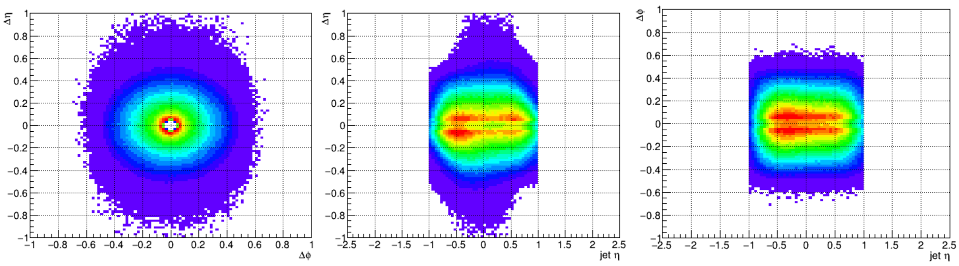

Figure 5.9: Two-dimensional distributions showing the correlations between $\Delta\eta$, $\Delta\phi$ and jet η at mixed events.

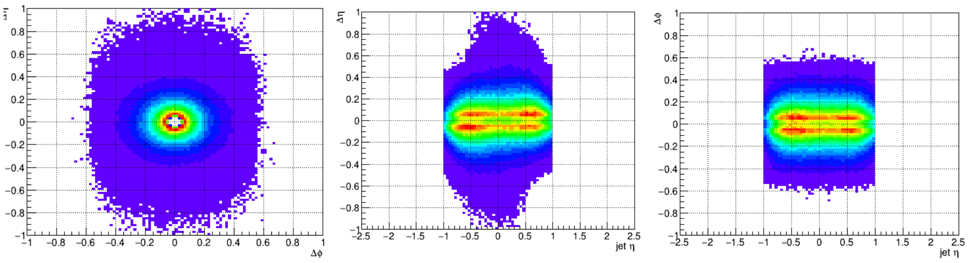

Figure 5.10: Two-dimensional distributions showing the correlations between $\Delta\eta$, $\Delta\phi$ and jet η at the same events.

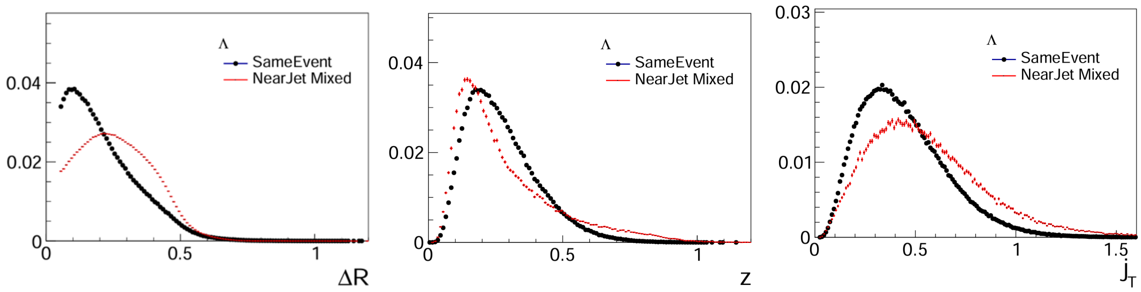

(a) ΔR between Λ and jet (b) Λ z distribution (c) Λ j_T distribution

Figure 5.11: Comparison of $\Delta R, z, j_T$ distribution of Λ between SameEvents and MixedEvents before reweighting.

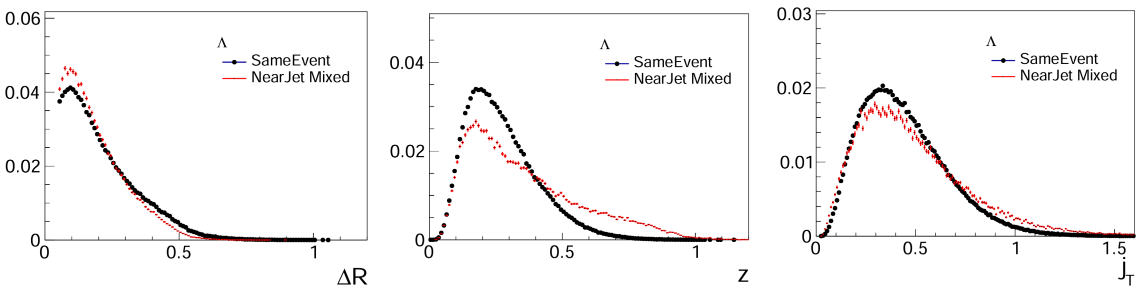

(a) ΔR between Λ and jet (b) Λ z distribution (c) Λ j_T distribution

Figure 5.12: Comparison of $\Delta R, z, j_T$ distribution of Λ between same events and mixed events after reweighting.

In addition, the Λ p_T distribution shows a discrepancy between same-event (SE) and mixed-event (ME) samples in Fig. 5.13, particularly in the high-p_T region. The 3D reweighting procedure not only failed to improve this inconsistency but even exacerbated it. However, as demonstrated in Fig. 5.15, the detector acceptance effect decreases with increasing Λ p_T. Combined with the relatively small fraction of high-p_T Λ particles, this discrepancy has no significant impact on the acceptance correction procedure.

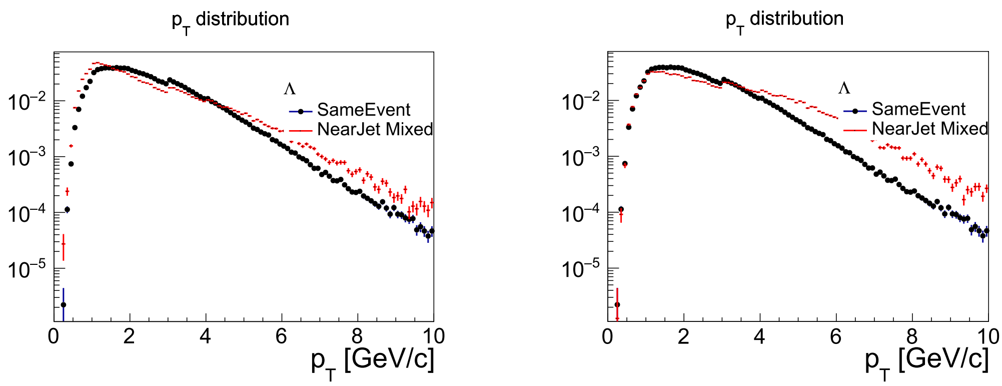

(a) Λ p_T before reweighting (b) Λ p_T after reweighting

Figure 5.13: Comparison of p_T distribution of Λ between same events and mixed events

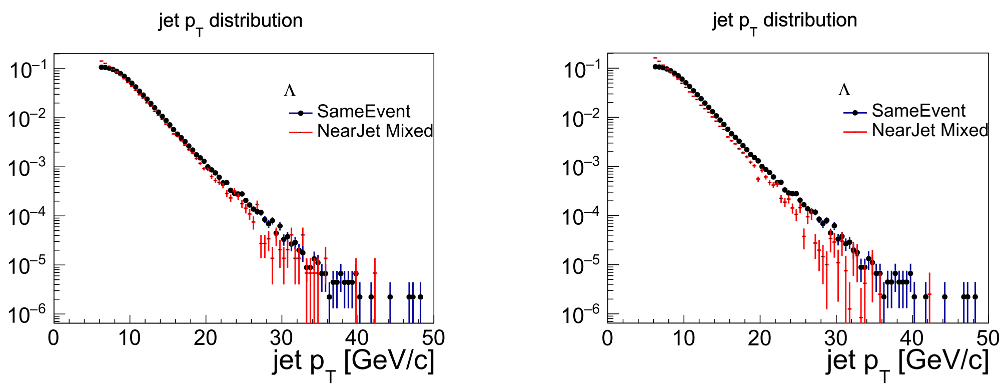

(a) Λ jet p_T before reweighting (b) Λ jet p_T after reweighting

Figure 5.14: Comparison of p_T distribution of Λ jet between same events and mixed events

The key consideration is whether the mixed-event method can adequately account for detector acceptance effects in our analysis. Figure 5.16(a) demonstrates that the mixed events successfully reproduce the $\cos\theta^*$ distribution, including acceptance effects, even *before* reweighting.

After applying the reweighting procedure, we observeed improved consistency in the $\cos\theta^*$ distribution, as evidenced by the ratio plot slope being compatible with zero (Figure 5.16(b)). This indicates that:

- The mixed-event sample introduces no artificial polarization signal
- Acceptance effects are properly modeled by the method

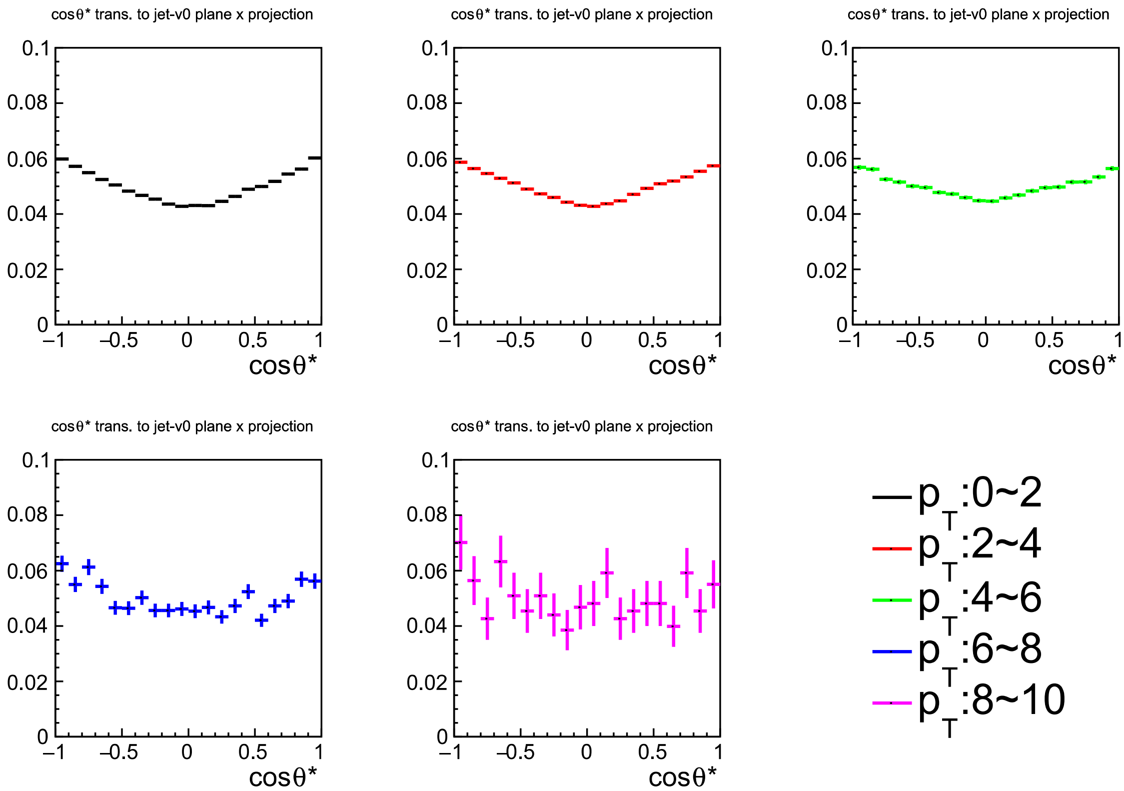

Figure 5.15: $\cos\theta^*$ distribution of in the different Λ p_T bins

However, this validation *does not* imply that the mixed-event technique can be directly applied to extract Λ polarization from polarized samples. The critical remaining question is how the mixed-event procedure affects the $\cos\theta^*$ distribution for *polarized* Λ hyperons - a key systematic uncertainty that must be quantified through:

$$\Delta P = P_{\text{true}} - P^{\text{(mixed events)}}_{\text{measured}} \tag{5.3}$$

where P denotes the polarization magnitude. This constitutes the final stage of our closure test and will determine the applicability limits of the method for this analysis.

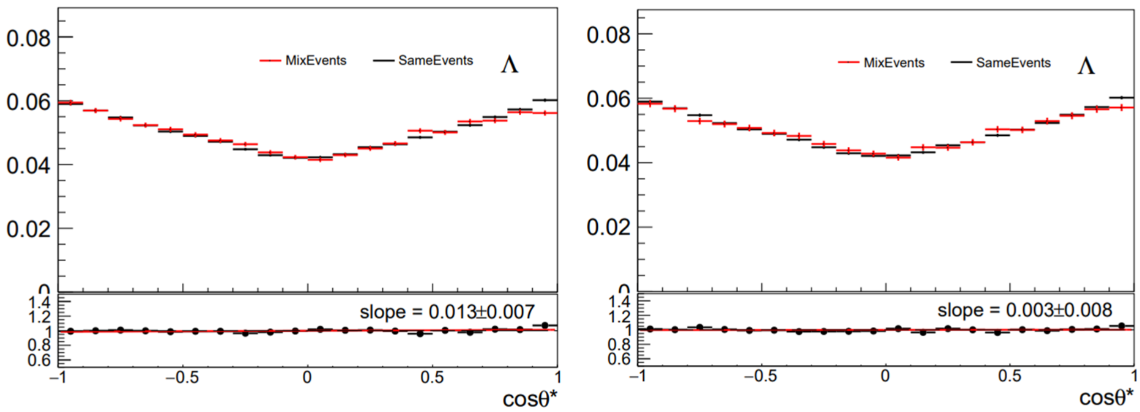

(a) $\cos\theta^*$ of Λ before reweighting

(b) $\cos\theta^*$ of Λ after reweighting

Figure 5.16: Comparison of $\cos\theta^*$ of Λ between same events and mixed events.

To confirm whether the mixed-event method works well in polarization extraction and how large impacts are for the polarized Λ sample, we generate a MC sample with polarized Λ by throwing some Λ randomly by a linear function of $\cos\theta^*$:

$$d\text{N}/d(\cos\theta^*) = (1 + \alpha P_\Lambda \cos\theta^*) \tag{5.4}$$

where P_Λ is the input polarization and α is the weak decay constant of Λ. The blue flat line in the left plot of Fig. 5.17 is $\cos\theta^*$ distribution with $P_\Lambda = 0$, and the red line is $\cos\theta^*$ distribution with $P_\Lambda = -0.1$. We fit this red line and get the same polarization signal as the input value. So we used the same method at the detector level. Then, we use this polarized lambda sample to make the mixed event.

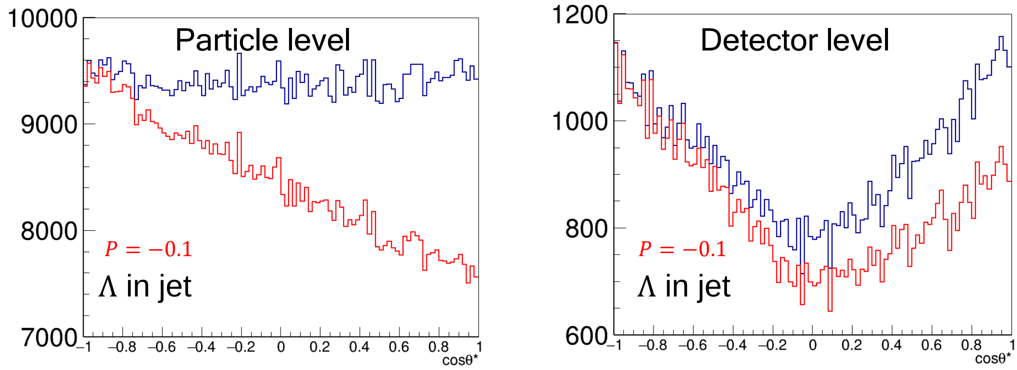

Figure 5.17: Left: cosθ^* of Λ at particle level. Right: cosθ^* of Λ at detector level

The validation of polarization extraction is presented in Fig. 5.18, showing the correlation between input (x-axis) and extracted (y-axis) Λ polarization values. The points are fitted with a linear function:

$$f(x) = p_0 x + p_1 \tag{5.5}$$

where p_0 and p_1 parameters denote the slope and y-intercept of the fit function, respectively.

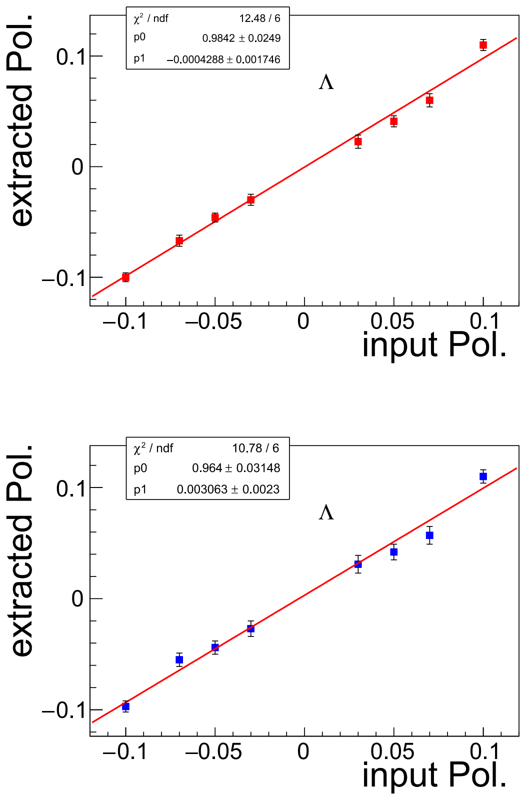

Figure 5.18: Extracted polarization vs input polarization of Λ; (Red points) before reweighting; (Blue points) after reweighting.

Notably, the extracted polarization values show excellent agreement with the input values both before and after reweighting, as evidenced by the goodness-of-fit ($\chi^2/\text{ndf} = 12.48/6$ $\chi^2/\text{ndf} = 10.78/6$). This consistency confirms the reliability of the mixed-event method for Λ polarization measurement. Furthermore, the observed discrepancy in the Λ p_T distribution does not have a significant impact on the acceptance correction procedure. The linear response with slope $p_1 = 0.96 \pm 0.03$ and intercept $p_0 = 0.003(2)\,\%$ demonstrates mixed events method and our reweighting procedure throughout the closure test without introducing significant systematic bias. The method properly accounts for detector acceptance variations and combinatorial background effects, with statistical uncertainties dominating the measurement precision while keeping systematic uncertainties below 7 %, making it fully suitable for precision measurements.

5.3 Mixed-events sample

A rigorous quality assessment (QA) of the mixed-event sample is essential prior to applying acceptance corrections. As previously discussed, this requires detailed comparison of kinematic distributions between mixed and single-event samples. Figure 5.19 shows the two-dimensional $\Delta\eta$ versus η_{jet} distribution for K_S^0 candidates, revealing significant discrepancies between mixed and same-event data. Most notably, the mixed events exhibit a pronounced $\Delta\eta$ asymmetry in opposite η_{jet} regions, which is absent in the genuine correlated events. To mitigate potential biases in the acceptance correction, we implemented the three-dimensional reweighting procedure ($\Delta\eta$, $\Delta\phi$, η_{jet}) described in Section 5.2.

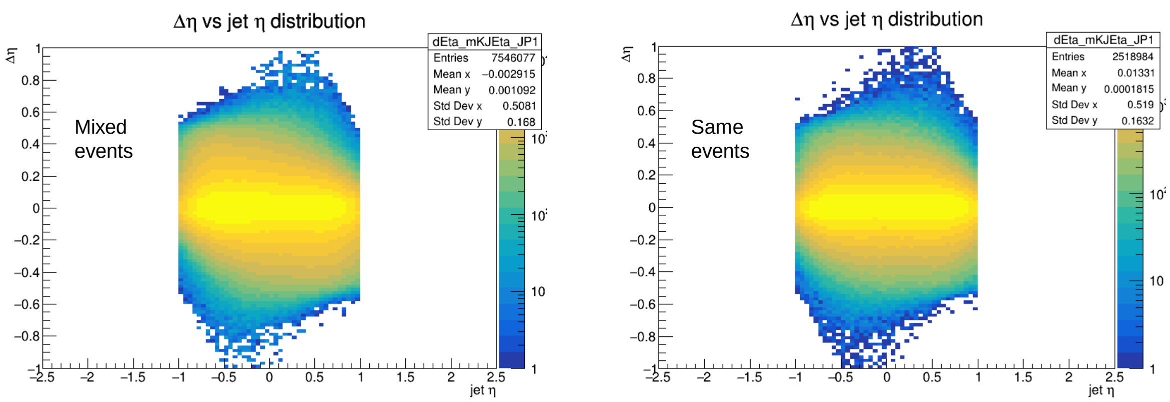

Figure 5.19: Left: $\Delta\eta$ vs η_{jet} in mixed events. Right: $\Delta\eta$ vs η_{jet} in same events.

The kinematic distributions, including pseudorapidity (η) and azimuthal angle (ϕ), remain well-preserved after reweighting, while inconsistency is observed in the transverse momentum (p_T) spectrum. However, studies confirm that this p_T discrepancy has no significant effect on the polarization extraction.

Additionally, we compare correlated observables between hyperons and jets after reweighting. The results show excellent agreement in the angular separation ΔR, while other variables exhibit slight deviations that resulted by the inconsistency of p_T. Nevertheless, these inconsistencies do not affect the acceptance correction, as verified by closure tests.

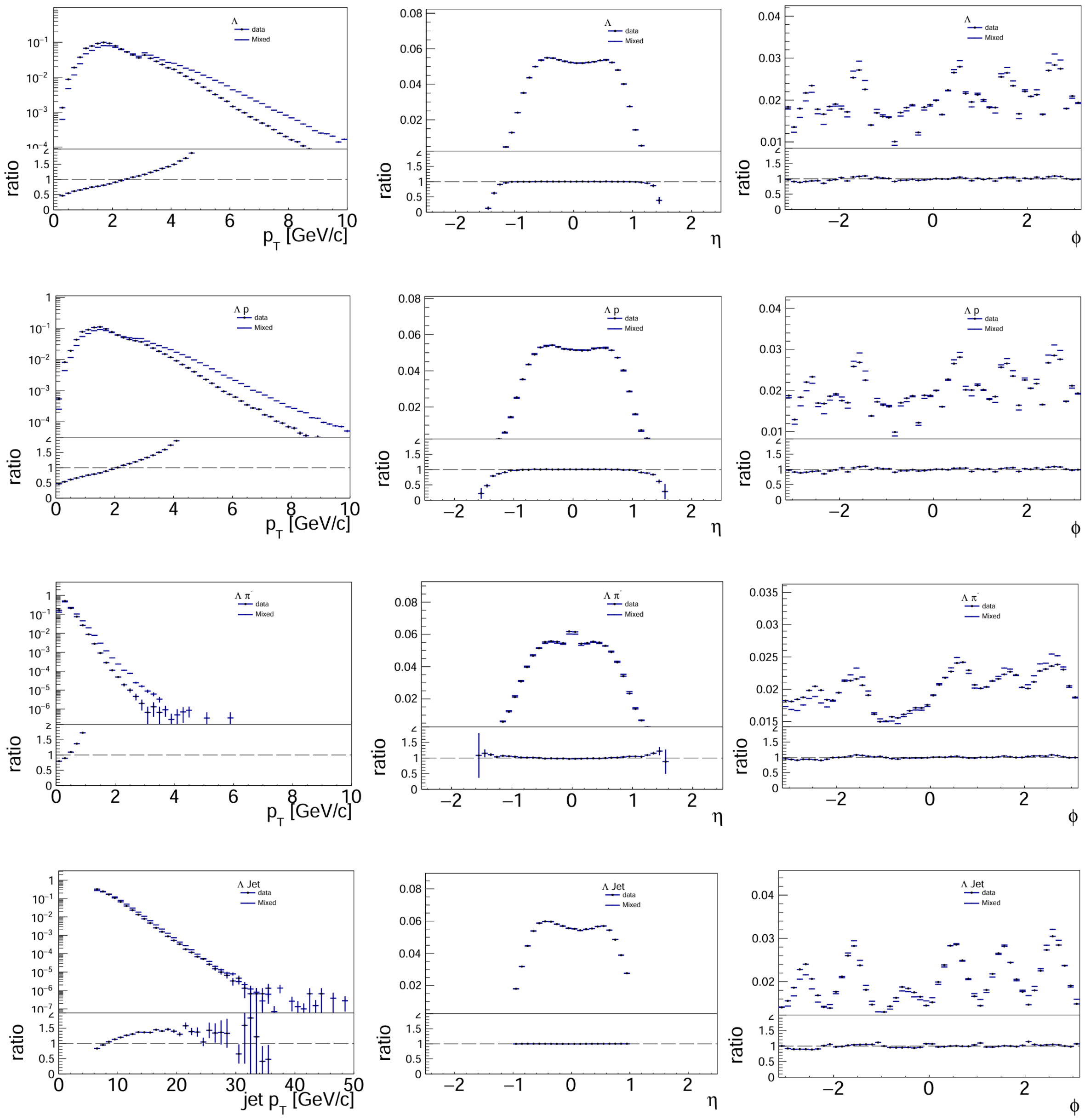

Figure 5.20: Comparisons of three kinematic quantities p_T, η, ϕ of Λ and jet between SE and ME.

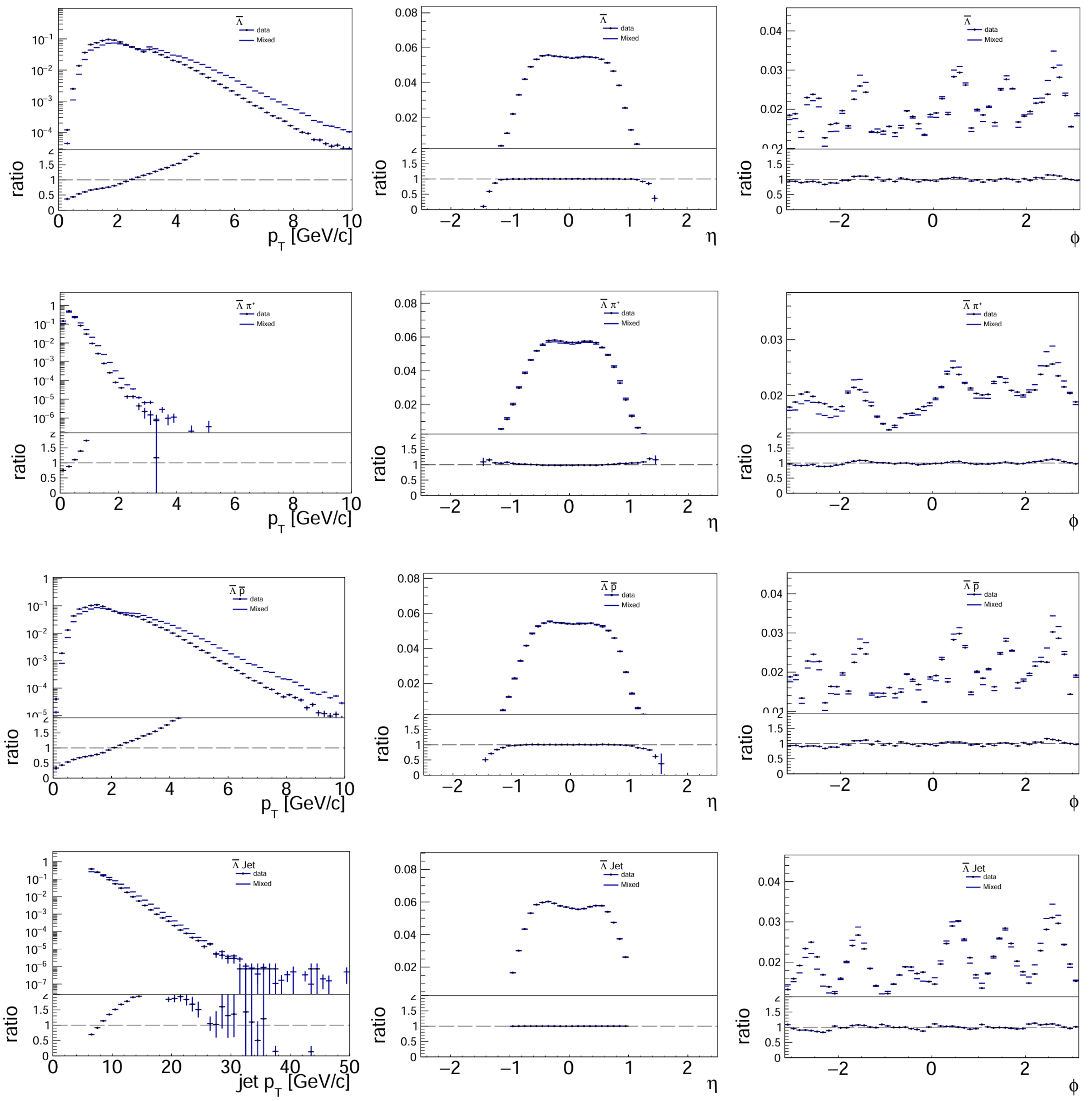

Figure 5.21: Comparisons of three kinematic quantities p_T, η, ϕ of $\overline{\Lambda}$ and jet between SE and ME.

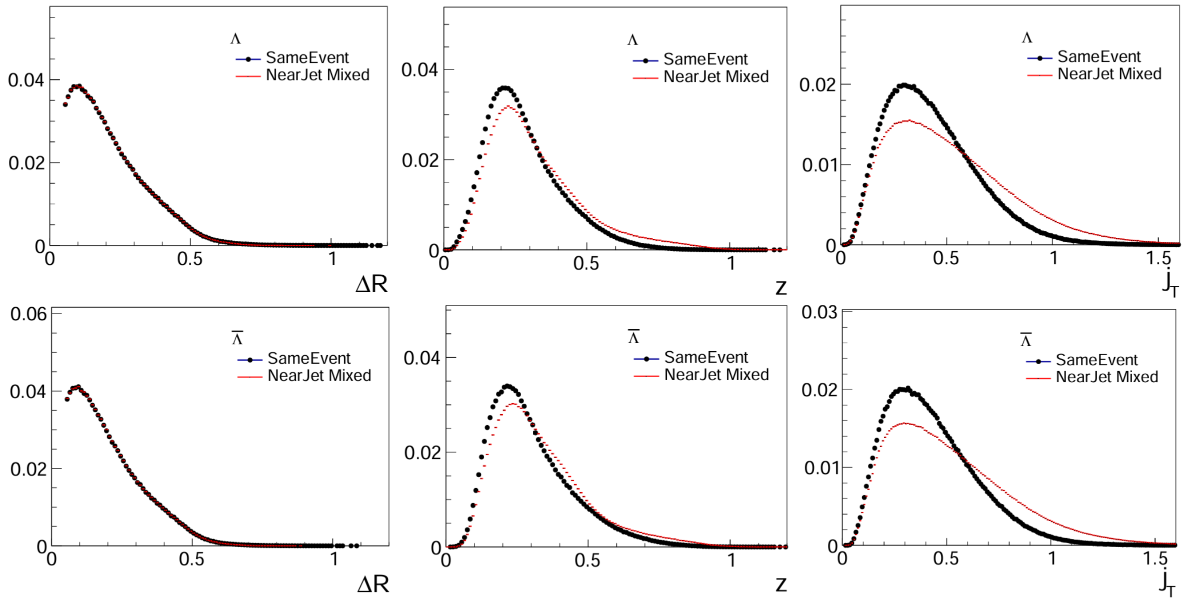

Figure 5.22: Comparisons of $\Delta R, z, j_T$ of Λ between SE and ME.

6 Transverse polarization $P_{\Lambda/\overline{\Lambda}}$ extraction of $\Lambda/\overline{\Lambda}$

6.1 Detector acceptance correction

Here shows the procedure of acceptance correction and lambda polarization extraction. The $\cos\theta^*$ distribution of Λ is not linear, as shown in Figure 6.1, which is attributed to the detector acceptance effects. Here, the mass peak window of the candidates Λ is set at $1.112 \sim 1.120$ GeV/c and background contribution had been subtracted from the $\cos\theta^*$ distribution under the mass peak using the sideband method, as shown in Figure 2.2.

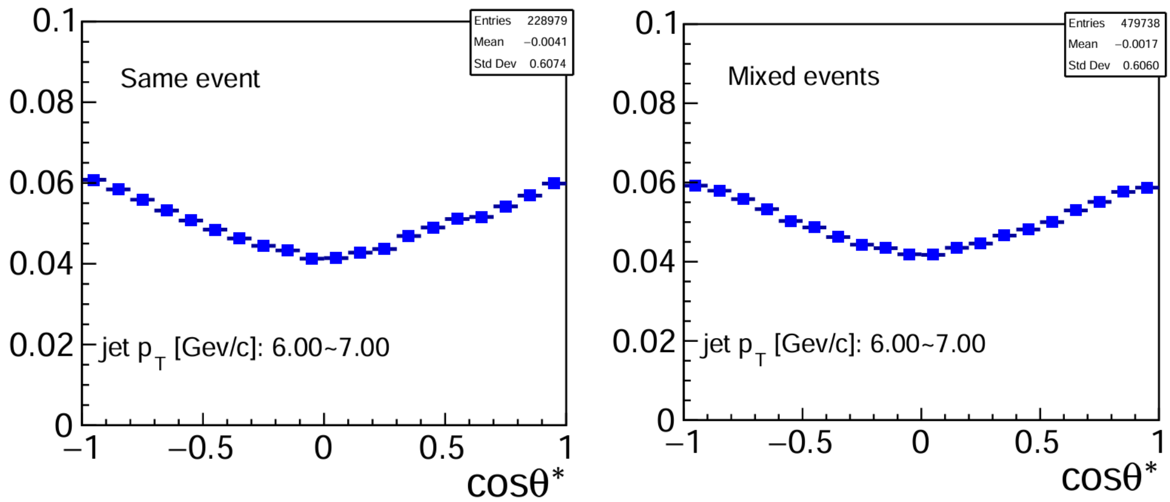

Figure 6.1: $\cos\theta^*$ distribution of Λ for the same event(left) and mixed events(right)

The acceptance correction can be done via mixed events. The cosθ^* distribution of Λ that could reflect detector acceptance can be seen in the right panel of Figure 6.1. The same background subtraction procedure was also applied for mixed events. Once the acceptance correction is done, polarization can be extracted by fitting the cosθ^* distribution with a linear function:

$$dN/d(\cos\theta^*) = A(\cos\theta^*)(1 + \alpha P_\Lambda \cos\theta^*) \tag{6.1}$$

where A(cosθ^*) denotes acceptance function. The α is the weak decay constant of Λ, which is $\alpha = 0.747 \pm 0.009$ [9]. The magnitude of weak decay constant for $\overline{\Lambda}$ is $\alpha = 0.757 \pm 0.004$.

Figure 6.2, as an example, shows the cosθ^* distribution of Λ after acceptance correction, and it was fitted by above function Eq. (6.1) to obtain polarization. The first fitting parameter p_0 is the extracted polarization. Its uncertainty from the fitting is treated as statistical uncertainty. Figure 6.3 and 6.4 show the fitting results at each jet bin for Λ and $\overline{\Lambda}$ respectively.

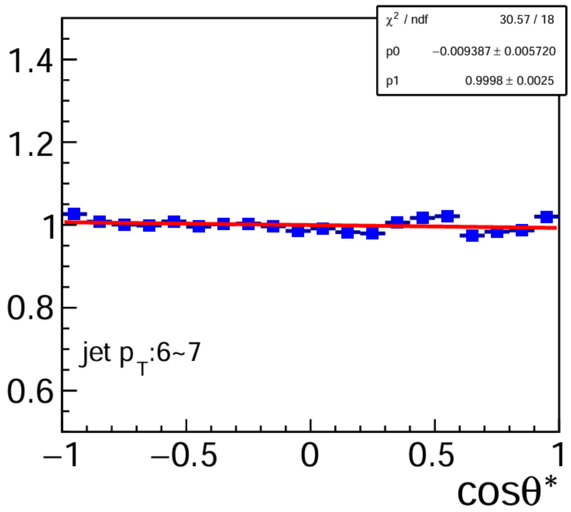

Figure 6.2: cosθ^* distribution of Λ after acceptance correction and was fitted with a linear function (red line) to extract polarization

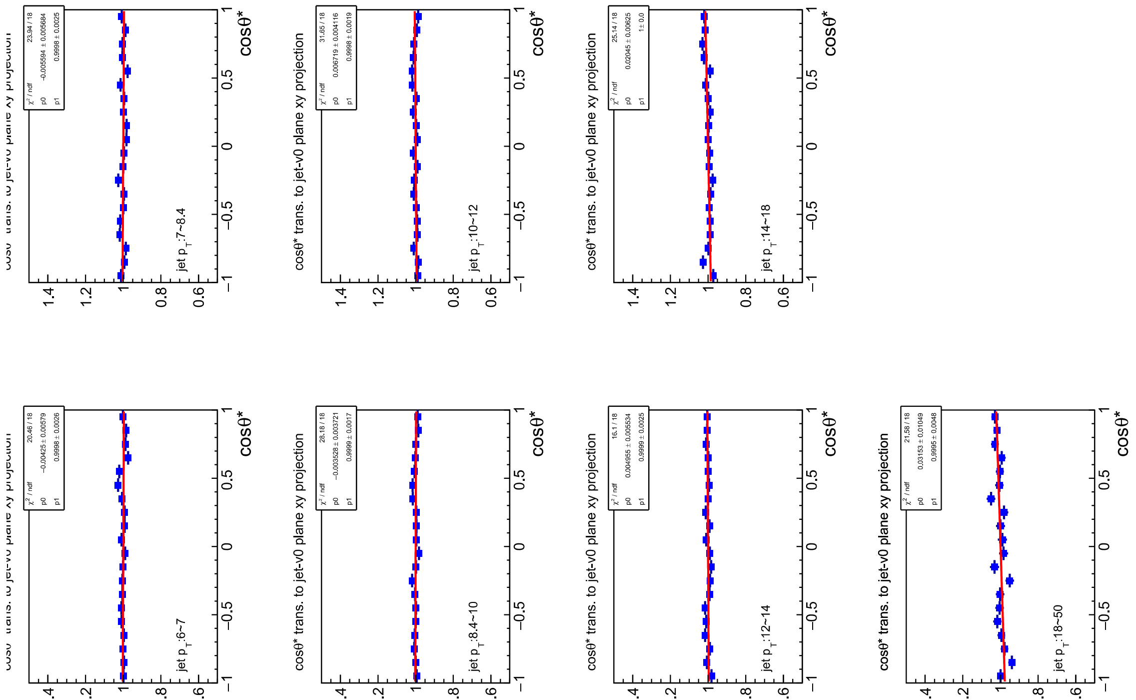

Figure 6.3: Extraction of transverse polarization of Λ as a function of jet p_T

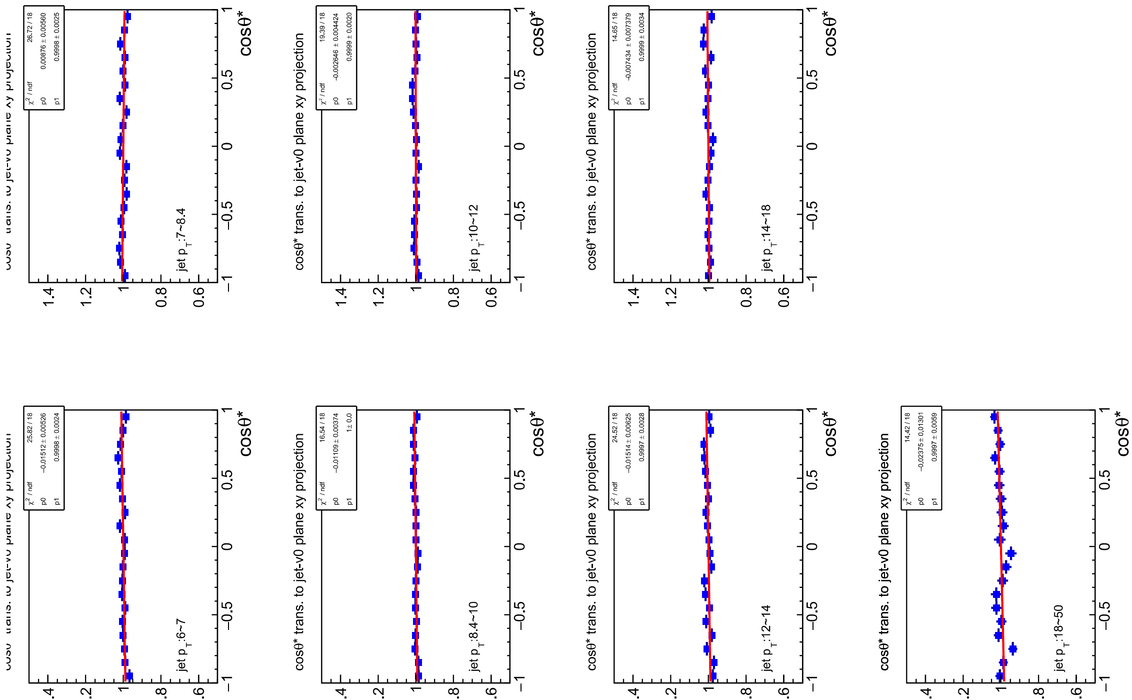

Figure 6.4: Extraction of transverse polarization of $\overline{\Lambda}$ as a function of jet p_T

6.2 Zero-test with K_s^0

In order to confirm the validity of polarization extraction of Λ and $\overline{\Lambda}$, the K_s^0 particle with zero spin is used to make zero-test. If extracted polarizations of K_s^0 are consistent with 0, it means the Λ and $\overline{\Lambda}$ polarizations extracted in this analysis are credible. The same procedure of polarization extraction is applied for K_s^0 particle. The transverse polarization of K_s^0 as a function of jet p_T is consistent with 0 as shown in Figure 6.5.

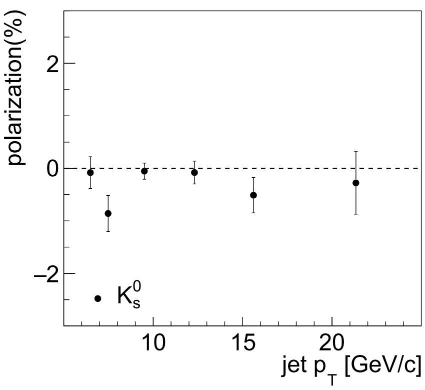

Figure 6.5: Transverse polarization of K_s^0 as a function of jet p_T

Besides, figure 6.6 and 6.7 present the transverse polarization of K_s^0 as a function of z and j_T. They are all consistent with 0 as expected, which means the method of polarization extraction in this analysis is credible.

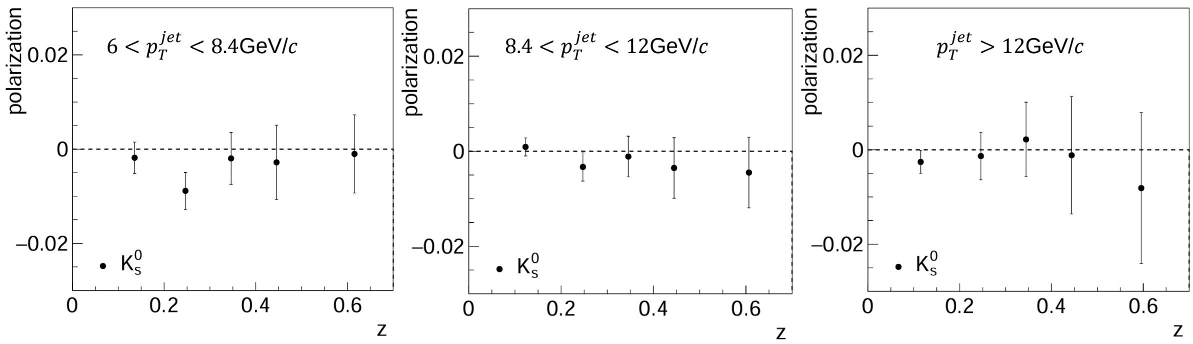

Figure 6.6: Transverse polarization of K_s^0 as a function of z at different jet p_T ranges

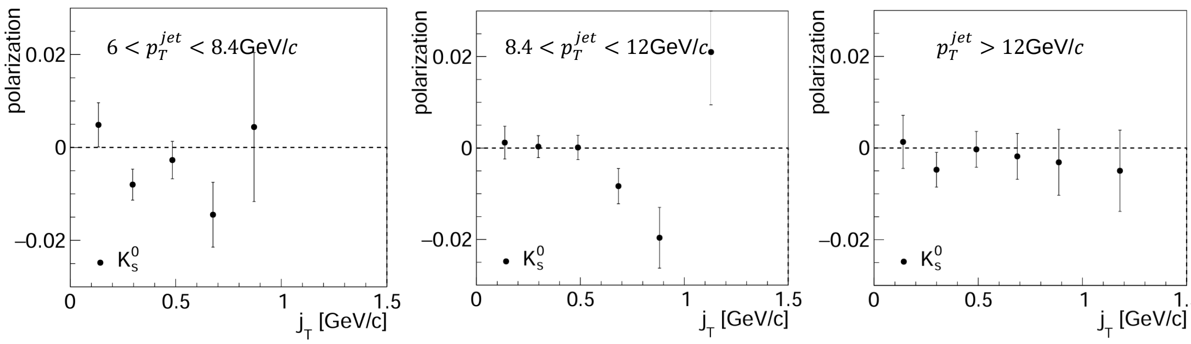

Figure 6.7: Transverse polarization of K_s^0 as a function of j_T at different jet p_T ranges

6.3 Comparison of results extracted by mixed events and MC

To validate our analysis results, we performed a systematic cross-check by comparing the polarization results obtained from two independent methods: mixed events and MC simulation incorporating detector response. Here show our JP1 results with the same selection criteria , which were extracted by MC simulation in Fig6.8 and by the mixed-events method. The trend of polarization that extracted by these two different methods are consistent.

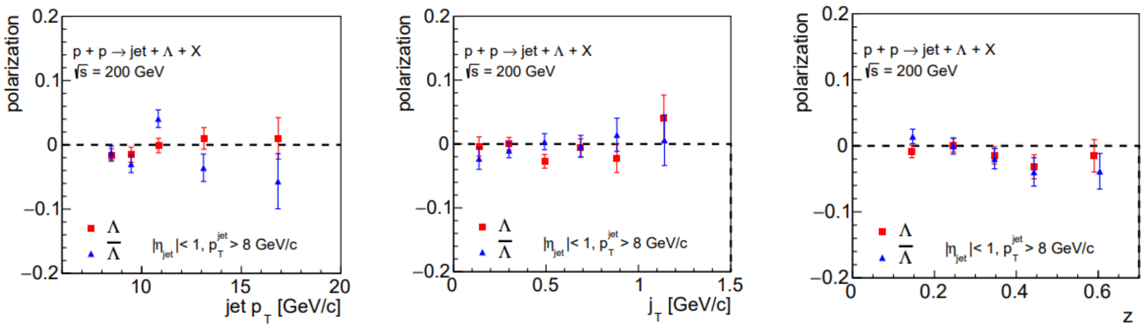

Figure 6.8: Transverse polarization extracted by MC

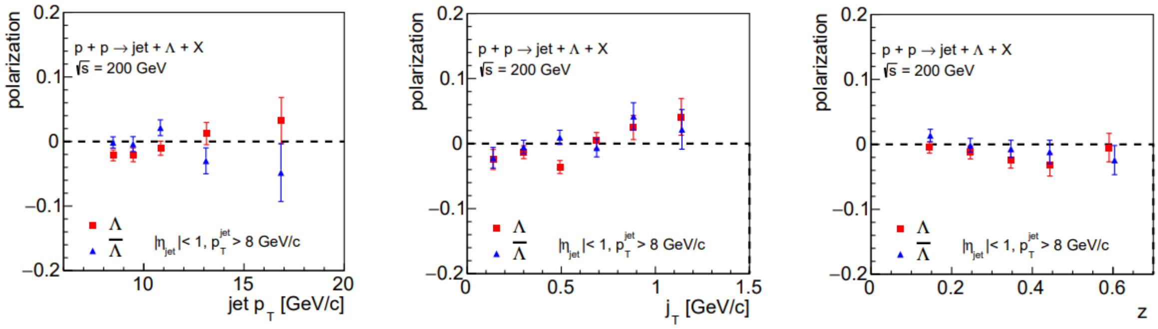

Figure 6.9: Transverse polarization extracted by mixed events

7 Correction for results

7.1 Polarization direction correction

The angular resolution of jet axis reconstruction is degraded by detector acceptance effects, directly impacting the determination of the polarization direction through the spin vector definition:

$$\hat{\boldsymbol{S}} = \hat{\boldsymbol{p}}_{\rm jet} \times \hat{\boldsymbol{p}}_{\Lambda} \tag{7.1}$$

where $\hat{\boldsymbol{p}}_{\rm jet}$ and $\hat{\boldsymbol{p}}_{\Lambda}$ represent the unit momentum vectors of the jet and Λ hyperon, respectively. As shown in the Fig.7.1, the angle $(\delta\theta)$ between true and detected polarization direction is resulted by the shift of jet axis, which will dilute Λ polarization signal. where the finite angular resolution can lead to:

- Misreconstruction of the polarization plane orientation
- Systematic shifts in the measured polarization magnitude
- Complete inversion of the polarization direction in extreme cases

This dilution effect becomes particularly significant for Λ candidates in close proximity to the jet axis. Fig.7.2 presents the ΔR dependence of cos$\delta\theta$. Apparently, the broadening of cos$\delta\theta$ distribution is large at samll ΔR $(\equiv \sqrt{(\Delta\phi)^2 + (\Delta\eta)^2})$ range, which should be 1 theoritical. ΔR is required to exceed 0.05 to ensure sufficient resolution in determining the Λ polarization direction. Hence, the final extracted polarization is component of true poalrization signal, which should be corrected by:

$$P_{\Lambda} = P_{det}/cos\delta\theta \tag{7.2}$$

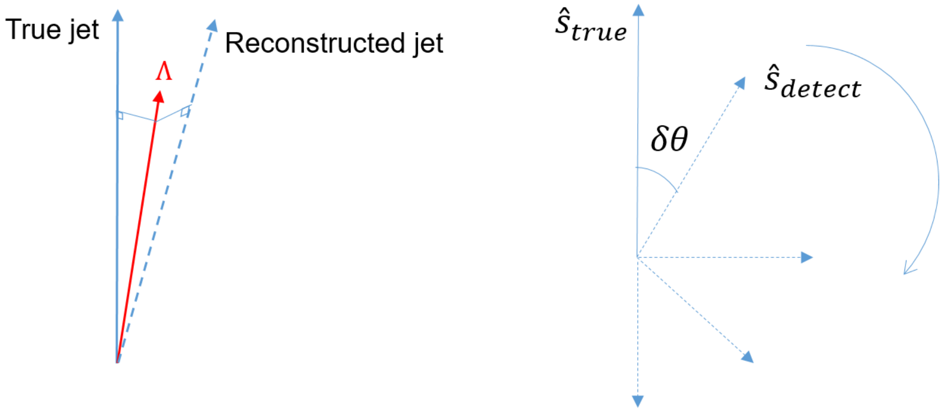

Figure 7.1: The resolution of reconstructed jet axis

We observed the significant jet p_T dependence of cos$\delta\theta$ distribution in the Fig.8.4. Therefore, it is necessary to make correction for the Λ polarization as function of jet p_T bin by bin. Here, we used the average value of cos$\delta\theta$ to make correction.

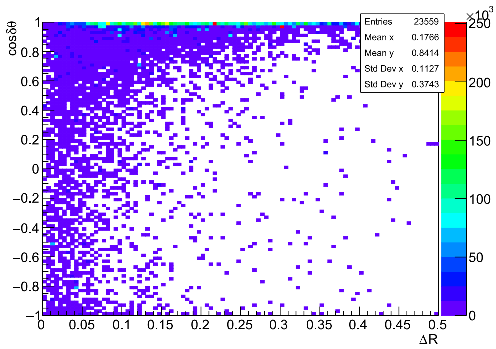

Figure 7.2: cos$\delta\theta$ vs ΔR

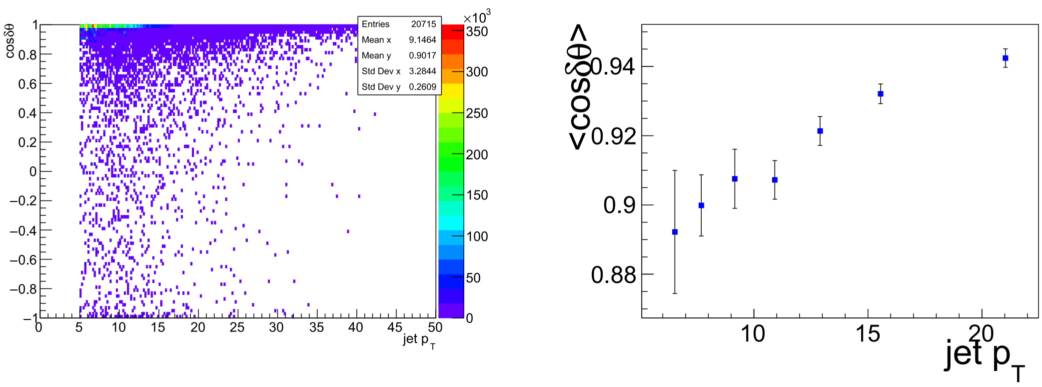

Figure 7.3: Left:cos$\delta\theta$ vs jet p_T; Right: the average of cos$\delta\theta$ vs jet p_T

7.2 Kinematic quantities correction

The finite resolution of the jet axis reconstruction induces shifts in the jet p_T and related kinematic variables, such as the momentum fraction z and transverse momentum relative to jet axis j_T. Figure 7.4 presents the resolution of these quantities (z, j_T, and jet p_T) as measured in the embedding sample. Here, the y-axis represents the particle-level (true) values, while the x-axis corresponds to the detector-level (reconstructed) measurements. We observe significant broadening in the distributions of these kinematic variables, indicating potential systematic shifts between the true and reconstructed values.

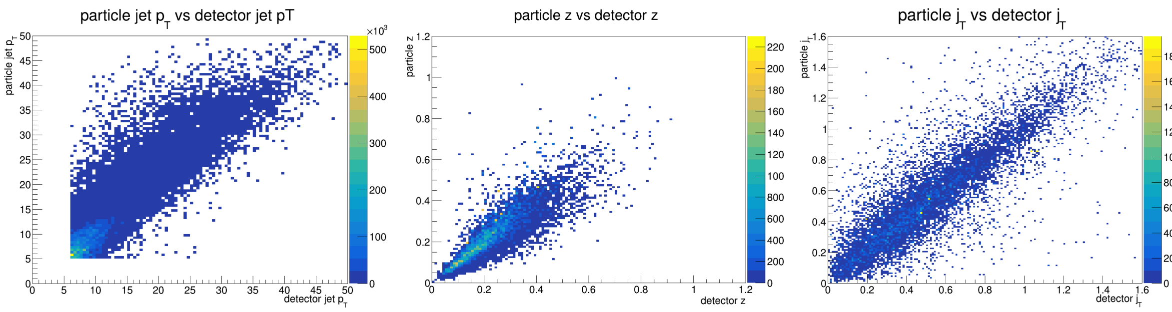

Figure 7.4: Particle-level versus detector-level

We performed linear fits to the mean particle-level values within corresponding detector-level (x-axis) ranges. Figure 7.5 demonstrates this linear correlation between particle-level and detector-level jet p_T. For the z and j_T variables, we divided their distributions into three distinct jet p_T regions matching those used in the final analysis. The fitting functions for these variables were more complex, as shown in Figure 7.6. These derived correction functions will be applied to account for reconstruction-induced shifts in the kinematic quantities.

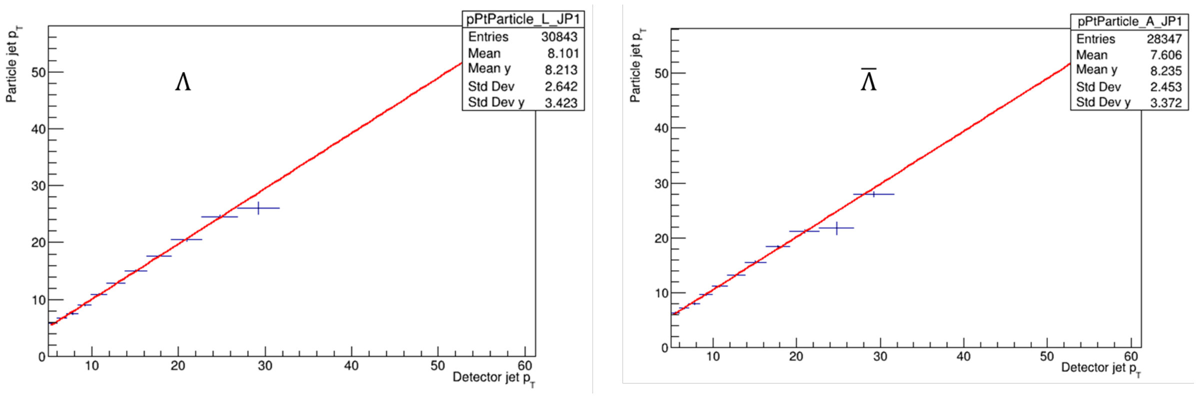

Figure 7.5: Shift corection for jet p_T

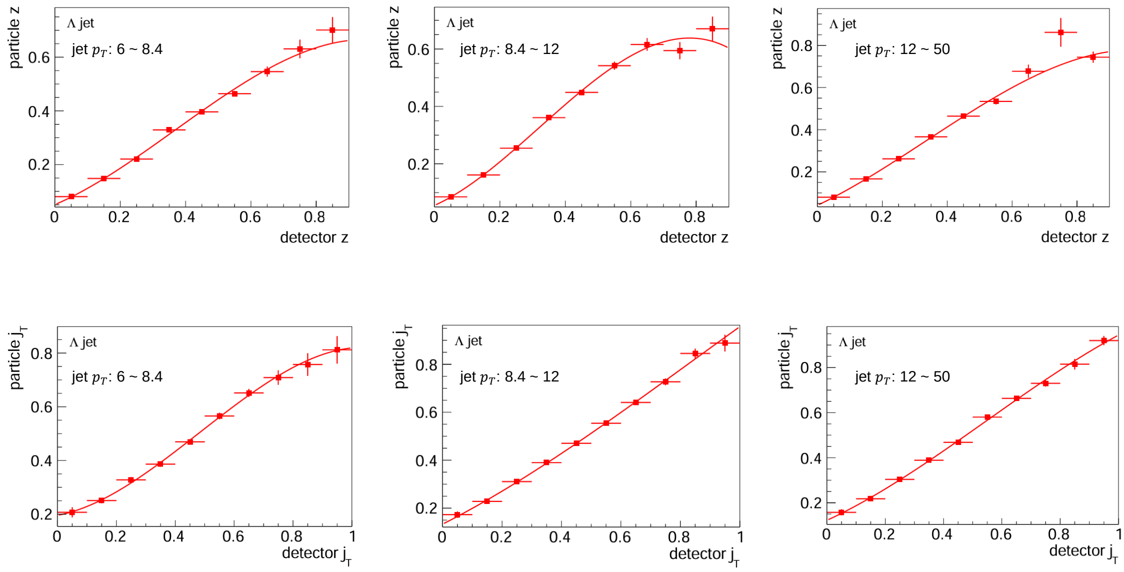

Figure 7.6: Shifts correction for z, j_T

8 Systematic uncertainties

Five sources of systematic uncertainties are taken into account. The first one is resulted from trigger effects, which will impact jet flavor and transverse momentum. The next systematic uncertainty originates from the variation of side-band range for background subtraction. The precision of decay parameter of Λ and $\overline{\Lambda}$ also contribute to the systematic uncertainties. The last one is contributed from the mixed event method.

8.1 Trigger Bias

In the data taking of STAR, trigger sets will impact jet transverse momentum and flavor fraction, especially at the edge of trigger threshold. This effect was simulated using embedding sample to estimate how large variation of jet flavor resulted by it. The two flavor fraction distributions at different jet p_T are presented at Fig. 8.1. The left plot is for no-bias sample and right one is for triggered sample. By comparing these two distributions from Fig. 8.1, the variation of quark fraction are used to estimate the systematic uncertainty with the following formula:

$$\sigma_{\text{trig}} = \left| \frac{f_{\text{nobias}} - f_{\text{trigger}}}{f_{\text{nobias}}} \right| \times \max(P_\Lambda, \sigma_{\text{stat}}), \tag{8.1}$$

where f_{nobias} and f_{trigger} are the sum of all quark fraction of no-bias sample and trigger-bias sample, respectively. Here, P_Λ is measured Λ polarization and σ_{stat} is statistical error of Λ polarization. In case σ_{trig} is too small as the measured Λ polarization is closed to zero, the maximum of P_Λ and σ_{stat} is applied to calculation.

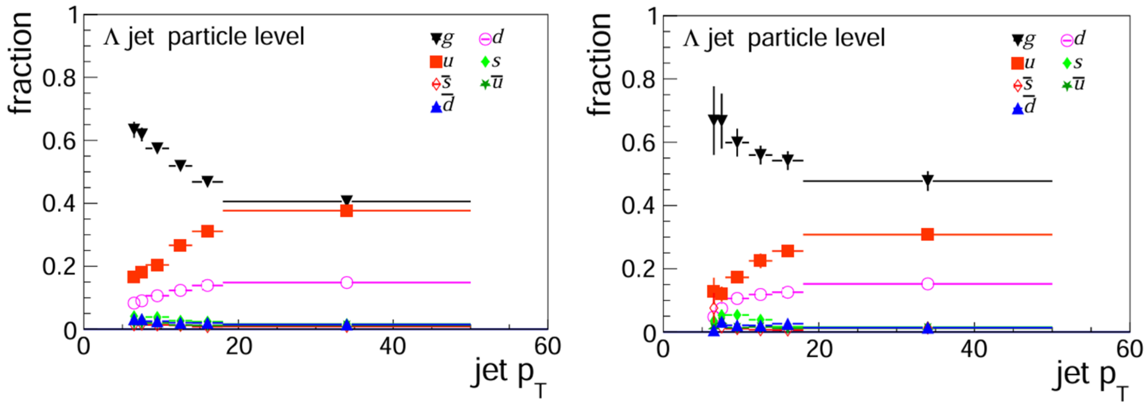

(a) Flavor fraction distribution without no-bias sample (b) Flavor fraction distribution with triggered sample

Figure 8.1: Flavor fraction distribution of Λ at different jet p_T.

8.2 Mixed event method

The second source comes from the ME correction in correcting the detector acceptance. A closure test is performed with the MC sample by manually putting a polarization signal into the generator level and then extract the polarization at detector level using the ME method. The extracted results are consistent with input value as shown before. The following figure 8.2 shows the relative difference $(((P_{out} - P_{in})/P_{in})$ and absolute difference $(P_{out} - P_{in})$ between them. We fitted 6 points from -0.07 to 0.07, which is close to the range of our polarization results, and obtain mean value of the relative differences up to 4.9% $\pm$4.4%. And average value of absolute viaration is 0.0009 ± 0.0019. The higher value 0.19% as a scale uncertainty is taken as systematic uncertainty.

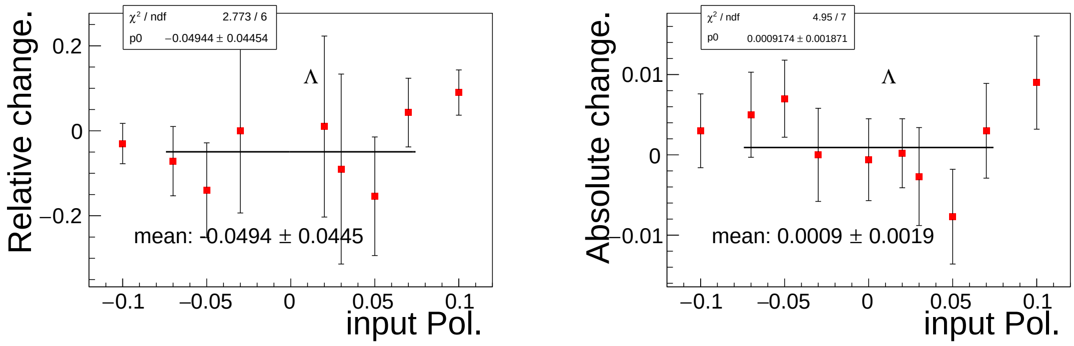

Figure 8.2: Relative change between inputted and extracted polarization.

8.3 Background estimation

The side-band method was applied to make background estimation and subtraction, as shown in Fig. 2.2. The background dN/d(cosθ) distribution is subtracted from dN/d(cosθ) distribution under Λ peak range. The estimated background varies with different choices of side-band region. Therefore, the choice of side-band will introduce a potential uncertainty to the measured polarization. This uncertainty is estimated by varying the side-band region. The polarizations are calculated with the varied side-band region and the maximum of change of P_Λ resulted by variation of side-band window are treated as the systematic uncertainties.

$$\sigma_{\rm bkg} = \Delta P_\Lambda = |\max(P_\Lambda - P_{bkg})| \tag{8.2}$$

where P_{bkg} is the extracted Λ polarization under varied side-band shift. And $\sigma_{\rm bkg}$ denotes background systematic uncertainty.

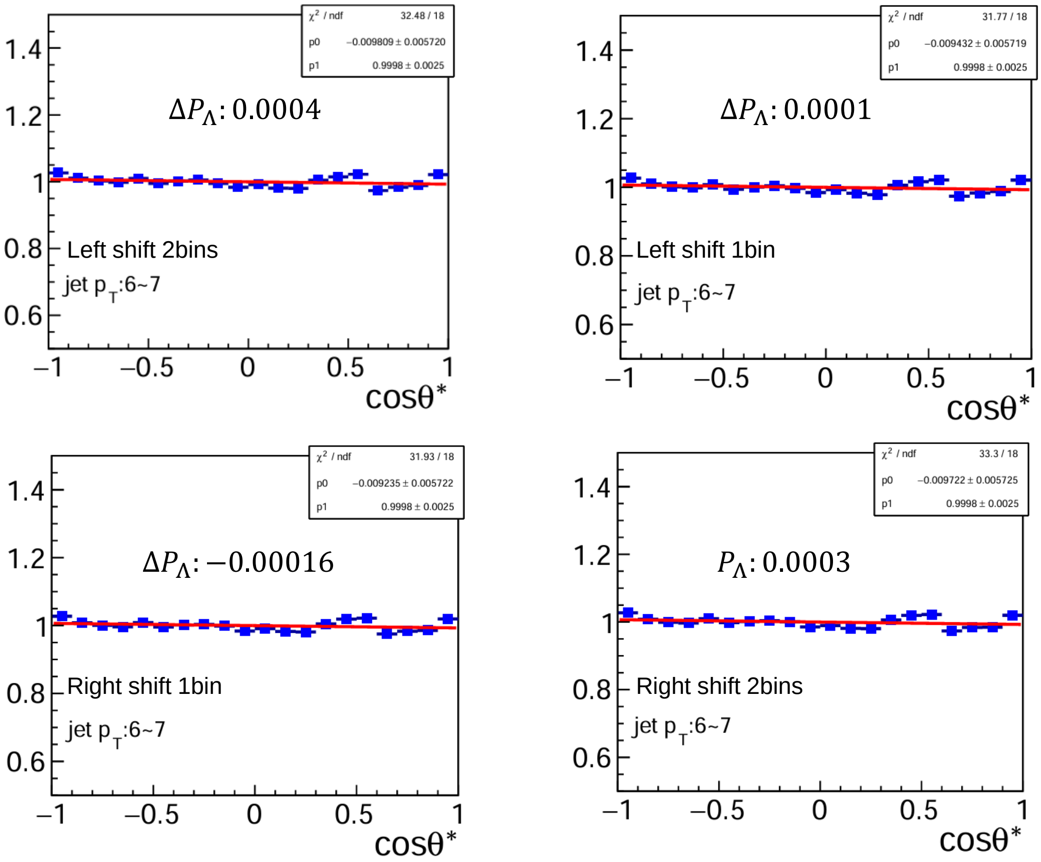

Figure 8.3: The extracted Λ polarization under varied side-band shift. The top two panels show polarization extraction under left shift of side-band, the bottom two panels show the polarization extraction under right shift of side-band.

8.4 The polarization direction correction

The precision of $\cos\delta\theta$, which is limited by the statistic of embedding sample, is also taken into account. The systematic uncertainties is calculated by the

$$\sigma_{\delta\theta} = \sigma_\theta / < cos\delta\theta > \times |P_\Lambda| \tag{8.3}$$

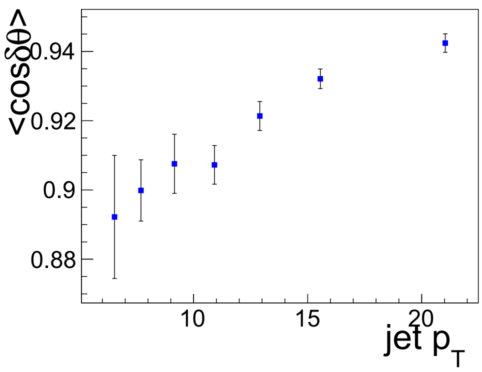

Figure 8.4: Left:cos$\delta\theta$ vs jet p_T; Right: the average of cos$\delta\theta$ vs jet p_T

8.5 Decay parameter

The last source of systematic uncertainties is from the precision of weak decay constants of Λ and $\overline{\Lambda}$. In this analysis, the weak decay constant α of Λ and $\overline{\Lambda}$ are: 0.747 ± 0.009 and -0.757 ± 0.004 respectively [9]. The systematic uncertainties from decay parameter relative to P_Λ is calculated by the following equation:

$$\sigma_\alpha = 0.009/0.747 \times |P_\Lambda| \tag{8.4}$$

The total systematic uncertainty σ_{sys} is calculated through following formula:

$$\sigma_{\text{sys}} = \sqrt{\sigma^2_{\text{trig}} + \sigma^2_{\text{bkg}} + \sigma^2_\alpha + \sigma^2_{\text{mix}} + \sigma^2_{\delta\theta}} \tag{8.5}$$

The systematic uncertainties σ_{sys} at different jet p_T range for Λ and $\overline{\Lambda}$ are summarized in Table 8.1 and 8.2 respectively. The systematic uncertainties for the polarization as the function of z and j_T are estimated with the same procedure.

			Λ				
jet p_T [GeV]	P_Λ	σ_{stat}	σ_{bkg}	σ_α	σ_{trig}	σ_{mixed}	σ_{sys}
6-7	-0.0098	0.0058	0.0007	0.0001	0.0009	0.0005	0.0012
7-8.4	-0.0089	0.0057	0.001	0.0001	0.0008	0.0004	0.0014
8.4-10	-0.0051	0.0038	0.0005	0.0001	0.0000	0.0003	0.0005
10-12	0.0025	0.0042	0.0012	0.0000	0.0007	0.0001	0.0014
12-14	-0.0002	0.0057	0.0004	0.0000	0.0002	0.0000	0.0005
14-18	0.0154	0.0065	0.001	0.0002	0.0021	0.0008	0.0025
18-50	0.0246	0.0113	0.0009	0.0003	0.003	0.0012	0.0033

Table 8.1: The table of Λ extracted polarization, statistical uncertainties and summary of systematic uncertainties at different jet p_T ranges

9 Results and conclusion

In this analysis, we measure the dependence of Λ and $\overline{\Lambda}$ transverse polarization on jet p_T, z and j_T.

				$\overline{\Lambda}$			
jet p_T [GeV]	$P_{\overline{\Lambda}}$	σ_{stat}	σ_{bkg}	σ_{α}	σ_{trig}	σ_{mixed}	σ_{sys}
6-7	-0.0165	0.0052	0.0007	0.0001	0.0015	0.0008	0.0019
7-8.4	0.0028	0.0056	0.001	0.0000	0.0005	0.0002	0.0012
8.4-10	-0.0125	0.0037	0.0005	0.0001	0.0001	0.0006	0.0008
10-12	-0.0057	0.0045	0.0012	0.0000	0.0009	0.0003	0.0015
12-14	-0.0208	0.0063	0.0004	0.0001	0.0008	0.001	0.0014
14-18	-0.0104	0.0075	0.001	0.0001	0.0015	0.0006	0.0019
18-50	-0.0299	0.0134	0.0009	0.0002	0.0036	0.0015	0.0040

Table 8.2: The table of $\overline{\Lambda}$ extracted polarization, statistical uncertainties and summary of systematic uncertainties at different jet p_T ranges

9.1 $P_{\Lambda/\overline{\Lambda}}$ vs jet p_T

Figure 9.1 shows the results of transverse polarization of Λ as a function of jet p_T. The red and blue markers denote Λ and $\overline{\Lambda}$ respectively. We can observe the significant transverse polarization of both Λ and $\overline{\Lambda}$ and clear jet p_T dependence. The Λ polarization increases with jet p_T and changes its sign from negative to positive at jet $p_T \sim 12$ GeV. The $\overline{\Lambda}$ polarization also increases with jet p_T but is always negative. In this figure, the vertical bars denote statistical uncertainties, and open boxes denote systematic uncertainties. The numerical values of the results are summarized in Tab. 9.1.

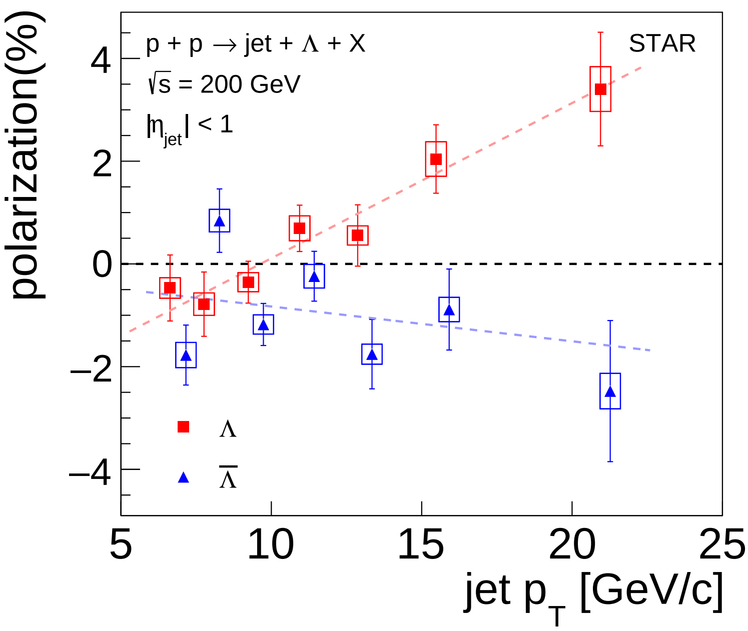

Figure 9.1: Transverse polarization of Λ and $\overline{\Lambda}$ as a function of jet p_T in unpolarized pp collisions at $\sqrt{s}$ =200 GeV at STAR. Statistical uncertainties are shown as vertical bars. Systematic uncertainties are shown as boxes.

	Λ				$\overline{\Lambda}$		
jet p_T [GeV]	P_Λ	$\sigma_{\rm stat}$	$\sigma_{\rm sys}$	jet p_T [GeV]	$P_{\overline{\Lambda}}$	$\sigma_{\rm stat}$	$\sigma_{\rm sys}$
6.4821	-0.0098	0.0058	0.0012	6.47	-0.0165	0.0052	0.0019
7.6453	-0.0089	0.0057	0.0014	7.627	0.0028	0.0056	0.0012
9.1596	-0.0051	0.0038	0.0005	9.1422	-0.0125	0.0037	0.0008
10.9155	0.0025	0.0042	0.0014	10.8958	-0.0057	0.0045	0.0015
12.9024	-0.0002	0.0057	0.0005	12.8898	-0.0208	0.0063	0.0014
15.586	0.0154	0.0065	0.0025	15.5532	-0.0104	0.0075	0.0019
21.2445	0.0246	0.0113	0.0033	21.1216	-0.0299	0.0134	0.0040

Table 9.1: The table of Λ and $\overline{\Lambda}$ extracted polarization, statistical uncertainties and summary of systematic uncertainties at different jet p_T ranges

9.2 $P_{\Lambda/\overline{\Lambda}}$ vs z and j_T

To provide further constraints for the pFFs, the transverse polarizations of Λ and $\overline{\Lambda}$ are also measured as functions of z and j_T, as shown in Figure 9.2 and 9.3. Because the Λ polarization as a function of jet p_T cross zero from negative to positive. There might be different z and j_T dependence of polarization at different jet p_T ranges. Hence, We separate jet p_T into three different ranges of: $6 < p_T^{jet} < 8.4$ GeV, $8.4 < p_T^{jet} < 12$ GeV and $p_T^{jet} > 12$ GeV, respectively. The polarizations of Λ and $\overline{\Lambda}$ show different z dependence at different jet p_T ranges. At low jet p_T range of $6 < p_T^{jet} < 8.4$ GeV, no clear z dependence of Λ or $\overline{\Lambda}$ polarization is observed. The polarization trend with z of Λ is similar to $\overline{\Lambda}$ at $8.4 < p_T^{jet} < 12$ GeV range. At high jet p_T range, the polarization of Λ and $\overline{\Lambda}$ become opposite and increase with z. But no j_T dependence of polarization is observed at these three jet p_T range.

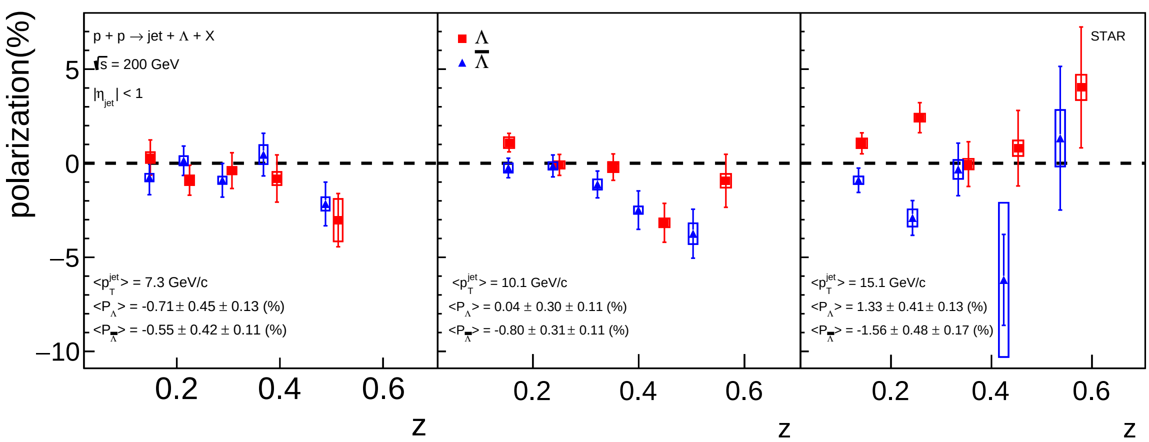

Figure 9.2: Transverse polarization of Λ,and $\overline{\Lambda}$ as a function of z at different jet p_T ranges of $6 < p_T^{jet} < 8.4$ GeV (left), $8.4 < p_T^{jet} < 12$ GeV (middle) and $p_T^{jet} > 12$ GeV (right). Statistical uncertainties are shown as vertical bars. Systematic uncertainties are shown as boxes.

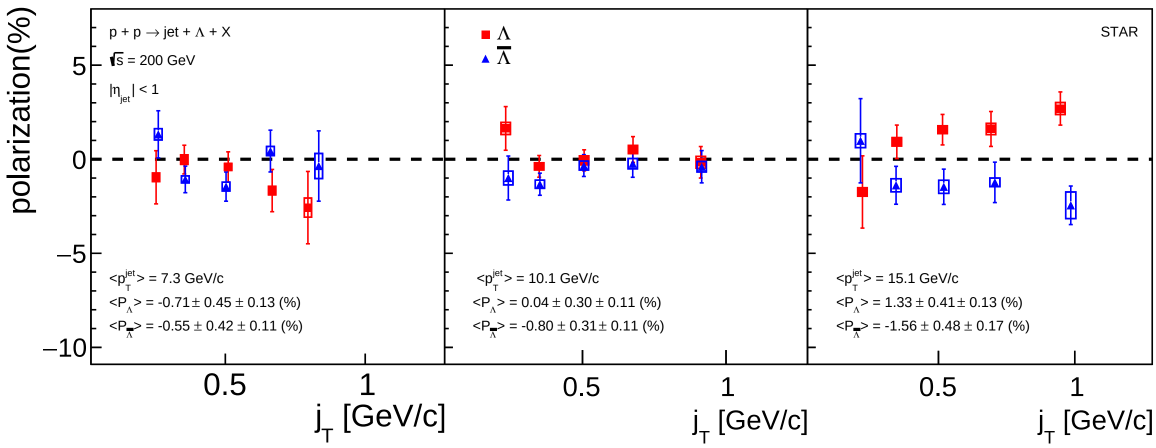

Figure 9.3: Transverse polarization of Λ,and $\overline{\Lambda}$ as a function of j_T at different jet p_T ranges of $6 < p_T^{jet} < 8.4$ GeV (left), $8.4 < p_T^{jet} < 12$ GeV (middle) and $p_T^{jet} > 12$ GeV (right). Statistical uncertainties are shown as vertical bars. Systematic uncertainties are shown as boxes.

$6 < p_T^{jet} \leq 8.4$				$8.4 < p_T^{jet} \leq 12$				$p_T^{jet} > 12$			
z	P_Λ	σ_{stat}	σ_{sys}	z	P_Λ	σ_{stat}	σ_{sys}	z	P_Λ	σ_{stat}	σ_{sys}
0.1528	0.0006	0.0085	0.0022	0.1426	0.0077	0.0044	0.0018	0.1243	0.0067	0.0053	0.0018
0.2484	-0.0099	0.0072	0.0020	0.2449	-0.004	0.0051	0.0008	0.2463	0.015	0.008	0.0012
0.3448	-0.0072	0.0087	0.0009	0.3459	-0.0036	0.0065	0.002	0.3432	0.0053	0.012	0.0023
0.4457	-0.0056	0.0113	0.003	0.4434	-0.0227	0.0094	0.0019	0.4424	0.0254	0.0193	0.0049
0.6033	-0.0251	0.0124	0.0103	0.5926	-0.0164	0.0124	0.0040	0.5908	0.0253	0.0291	0.0059
z	$P_{\overline{\Lambda}}$	σ_{stat}	σ_{sys}	z	$P_{\overline{\Lambda}}$	σ_{stat}	σ_{sys}	z	$P_{\overline{\Lambda}}$	σ_{stat}	σ_{sys}
0.157	-0.0076	0.0083	0.0010	0.1229	0.0035	0.0019	0.0022	0.1251	-0.0104	0.0061	0.0011
0.2491	-0.0042	0.007	0.0017	0.247	-0.0017	0.003	0.0009	0.2463	-0.0288	0.0088	0.0047
0.3458	-0.016	0.0081	0.0012	0.3454	0.0001	0.0043	0.0020	0.343	-0.019	0.0133	0.0063
0.4464	0.0037	0.0101	0.0047	0.4445	-0.0023	0.0064	0.0014	0.442	-0.0556	0.022	0.0397
0.6198	-0.013	0.01	0.0022	0.6065	-0.0044	0.0074	0.0047	0.6071	-0.0415	0.0343	0.0172

Table 9.2: The table of Λ and $\overline{\Lambda}$ extracted polarization, statistical uncertainties and summary of systematic uncertainties at different z ranges

9.3 Conclusions

- Our analysis is the first measurement of transverse polarization of Λ and $\overline{\Lambda}$ within jet in unpolarized pp collisions at $\sqrt{s}$ =200 GeV.
- Significant polarizations of Λ and $\overline{\Lambda}$ are observed with clear dependence on jet p_T.
- The z and j_T dependence of polarization are measured, and visible z dependencies are observed for medium to high jet p_T.
- These measurements provide important constraints on polarizing Fragmentation Functions.

$6 < p_T^{jet} \leq 8.4$				$8.4 < p_T^{jet} \leq 12$				$p_T^{jet} > 12$			
j_T	P_Λ	σ_{stat}	σ_{sys}	j_T	P_Λ	σ_{stat}	σ_{sys}	j_T	P_Λ	σ_{stat}	σ_{sys}
0.1345	-0.0159	0.0105	0.0016	0.136	0.011	0.0083	0.0025	0.1381	-0.0068	0.0134	0.0014
0.2993	-0.0004	0.0069	0.0018	0.3006	-0.0067	0.0052	0.0009	0.3014	0.0086	0.0081	0.0014
0.49	-0.0047	0.0073	0.0004	0.4926	-0.0032	0.0051	0.0016	0.494	0.0112	0.0076	0.0010
0.6821	-0.0204	0.0103	0.0017	0.6873	0.0026	0.0063	0.0012	0.6901	0.0119	0.0087	0.0023
0.9026	-0.0238	0.0176	0.0050	0.9506	-0.008	0.0078	0.0028	1.006	0.017	0.0084	0.0021
j_T	$P_{\overline{\Lambda}}$	σ_{stat}	σ_{sys}	j_T	$P_{\overline{\Lambda}}$	σ_{stat}	σ_{sys}	j_T	$P_{\overline{\Lambda}}$	σ_{stat}	σ_{sys}
0.1349	0.0047	0.0092	0.0019	0.1366	-0.0129	0.0083	0.0038	0.1376	-0.0139	0.0155	0.0032
0.2985	-0.0125	0.0063	0.0008	0.3009	-0.0114	0.0053	0.0013	0.3023	-0.0212	0.0091	0.0048
0.4898	-0.0153	0.007	0.0019	0.4928	-0.0065	0.0053	0.0019	0.4947	-0.0164	0.0087	0.0036
0.6831	0.0015	0.0102	0.0017	0.6882	-0.0059	0.0066	0.0021	0.6909	-0.0162	0.01	0.0017
0.9057	-0.0072	0.0171	0.0065	0.9597	-0.0103	0.0079	0.0026	1.0123	-0.0247	0.0097	0.0075

Table 9.3: The table of Λ and $\overline{\Lambda}$ extracted polarization, statistical uncertainties and summary of systematic uncertainties at different z ranges

References

[1] T. D. Lee and C. N. Yang, Phys. Rev. **108**, 1645 (1957).

[2] M. I. Abdulhamid et al. [STAR collaboration], Phys. Rev. D **109**, 012004 (2024) Ming Shao et al. PRC 75, 064901 (2007)

[3] Ming Shao et al. Phys. Rev. C **75**, 064901 (2007)

[4] B. Abelev et al. [ALICE Collaboration], Phys. Rev. D **91**, 112012 (2015).

[5] M. Cacciari, G. P. Salam, and G. Soyez, Eur. Phys. J. C **72**, 1896 (2012).

[6] T. Sjostrand, S. Mrenna and P.Z. Skands, PYTHIA 64 physics and manual, JHEP 05 026 (2006).

[7] R Brun et al. Report No.CERN-DD-EE-84-1 (1987)

[8] S.F. Pate et al. JINST **18** P10032 (2023)

[9] Zyla, P.A., et al. [Particle Data Group], The Review of Particle Physics, Phys. Rev. D **110**, 030001 (2024)

Appendices

16042102 16045032 16046016 16048002 16050070 16052022 16053065 16055127 16058080
16060042 16062018 16042103 16045033 16046017 16048003 16050071 16052023 16053066
16055128 16058082 16060043 16062019 16042105 16045043 16046018 16048004 16050072
16052028 16053067 16055129 16058083 16060044 16062020 16042116 16045044 16046019
16048009 16050073 16052030 16053073 16055130 16058084 16060045 16062021 16042117
16045045 16046020 16048014 16050075 16052031 16053074 16055131 16058085 16060046
16062022 16042118 16045047 16046021 16048015 16050076 16052032 16053075 16055132
16058086 16060053 16062023 16042126 16045048 16046032 16048016 16051001 16052034
16053077 16055133 16058087 16060054 16062024 16043002 16045049 16046033 16048017
16051003 16052035 16053078 16055134 16058088 16060055 16062025 16043004 16045052
16046034 16048018 16051004 16052036 16053079 16056004 16058089 16060056 16062045
16043006 16045054 16046035 16048019 16051007 16052037 16054001 16056016 16058090
16060057 16062046 16043007 16045055 16046036 16048022 16051008 16052038 16054005
16056017 16058091 16060058 16062047 16043009 16045056 16046037 16048023 16051009
16052039 16054006 16056018 16058093 16060059 16062049 16043013 16045067 16046038
16048024 16051022 16052040 16054007 16056019 16058095 16060060 16062050 16043016
16045068 16046039 16048025 16051026 16052041 16054010 16056022 16058096 16060061
16062051 16043019 16045070 16046040 16048026 16051027 16052042 16054011 16056023
16058100 16060062 16062052 16043020 16045082 16046041 16048027 16051028 16052043
16054012 16057003 16059011 16060063 16062053 16043021 16045083 16046042 16048028
16051029 16052044 16054013 16057004 16059012 16060064 16062054 16043022 16045084
16046043 16048109 16051030 16052045 16054014 16057005 16059013 16060065 16062055
16043024 16045085 16046044 16048110 16051031 16052046 16054018 16057006 16059015
16061008 16062056 16043026 16045086 16046045 16048111 16051032 16052048 16054019
16057007 16059016 16061009 16062057 16043031 16045087 16046046 16048115 16051033
16052049 16054020 16057008 16059017 16061010 16062058 16043033 16045088 16046048
16048116 16051034 16052050 16054022 16057009 16059018 16061011 16062078 16043035
16045089 16046049 16048117 16051035 16052051 16054059 16057010 16059019 16061012
16063001 16043037 16045090 16046050 16048118 16051036 16052087 16054060 16057011
16059022 16061013 16063002 16043079 16045093 16046057 16048119 16051037 16052088
16054061 16057012 16059024 16061014 16063003 16043082 16045094 16046058 16048120
16051038 16052089 16054062 16057013 16059025 16061015 16063004 16043084 16045095
16046059 16048121 16051039 16053001 16054063 16057016 16059026 16061016 16063005
16043085 16045096 16046061 16048122 16051040 16053002 16054064 16057017 16059027
16061017 16063006 16043086 16045097 16046062 16048125 16051041 16053003 16054069
16057018 16059030 16061018 16063007 16043089 16045098 16046064 16048126 16051042
16053004 16054070 16057046 16059031 16061019 16063091 16043091 16045099 16046065
16048127 16051044 16053005 16054072 16057047 16059041 16061035 16063092 16043092
16045100 16046066 16048128 16051045 16053006 16054073 16057048 16059062 16061037
16063093 16043096 16045102 16046067 16049010 16051046 16053007 16054074 16057049
16059064 16061038 16063094 16043105 16045103 16046073 16049012 16051047 16053008
16054075 16057050 16059065 16061039 16063095 16043106 16045104 16046074 16049013
16051048 16053009 16054077 16057051 16059066 16061041 16063096 16044017 16045105
16046075 16049017 16051049 16053010 16054078 16057053 16059067 16061042 16063097
16044019 16045106 16046076 16049018 16051050 16053011 16054079 16058001 16059068

16061049 16063099 16044022 16045108 16046077 16049020 16051051 16053012 16054080
16058002 16059069 16061060 16063100 16044023 16045109 16046078 16049022 16051052
16053017 16054082 16058005 16060001 16061061 16063111 16044027 16045110 16046080
16049023 16051056 16053019 16054086 16058006 16060002 16061062 16063112 16044028
16045111 16046081 16049024 16051057 16053030 16054087 16058007 16060003 16061075
16063113 16044029 16045112 16046082 16049025 16051058 16053031 16055002 16058008
16060004 16061076 16064001 16044030 16045113 16046083 16050009 16051059 16053043
16055003 16058015 16060005 16061077 16064002 16044033 16045114 16047004 16050010
16051060 16053044 16055004 16058016 16060008 16061078 16064006 16044036 16045115
16047005 16050036 16051101 16053045 16055005 16058017 16060011 16061083 16064007
16044037 16045116 16047008 16050037 16051102 16053046 16055007 16058018 16060014
16061084 16064008 16044038 16045117 16047101 16050038 16051103 16053047 16055010
16058019 16060016 16062001 16064009 16044046 16045118 16047102 16050039 16051104
16053048 16055011 16058020 16060017 16062002 16064010 16044047 16045119 16047103
16050040 16051105 16053049 16055012 16058021 16060018 16062003 16064013 16044050
16045120 16047104 16050041 16051106 16053051 16055013 16058022 16060026 16062004
16064017 16044061 16046003 16047106 16050042 16051107 16053052 16055018 16058023
16060027 16062005 16064018 16044110 16046005 16047108 16050043 16051108 16053053
16055019 16058024 16060028 16062006 16064019 16044111 16046006 16047121 16050044
16051109 16053054 16055021 16058025 16060030 16062008 16044112 16046007 16047122
16050048 16051110 16053055 16055022 16058026 16060031 16062009 16044114 16046008
16047124 16050049 16051111 16053056 16055024 16058070 16060032 16062010 16044115
16046009 16047125 16050050 16052013 16053057 16055025 16058071 16060034 16062011
16044120 16046010 16047126 16050051 16052015 16053058 16055120 16058072 16060036
16062012 16044123 16046011 16047131 16050052 16052016 16053059 16055121 16058073
16060037 16062013 16044133 16046012 16047136 16050053 16052017 16053060 16055122
16058074 16060038 16062014 16044138 16046013 16047137 16050054 16052018 16053062
16055123 16058077 16060039 16062015 16044139 16046014 16047138 16050065 16052019
16053063 16055124 16058078 16060040 16062016 16045001 16046015 16048001 16050066
16052021 16053064 16055125 16058079 16060041 16062017

16065023 16067016 16069064 16073013 16078041 16080043 16082050 16085032 16087021
16089020 16091009 16065024 16067017 16069065 16073017 16078042 16080045 16082051
16085033 16087022 16089024 16091010 16065025 16067019 16069067 16073018 16078056
16080046 16082052 16085035 16087023 16089026 16091011 16065026 16067020 16070003
16073019 16079001 16080047 16082053 16085036 16087024 16089027 16091012 16065027
16067021 16070004 16073020 16079010 16080048 16082054 16085037 16087025 16089028
16091013 16065028 16067022 16070005 16073021 16079011 16080049 16082055 16085051
16087026 16089029 16091014 16065036 16067040 16070006 16073029 16079013 16080050
16082056 16085052 16087027 16089030 16091061 16065037 16067041 16070008 16073030
16079014 16080051 16082057 16085054 16087028 16089031 16091062 16065038 16067042
16070009 16073031 16079015 16080052 16083005 16085055 16087029 16089041 16091063
16065039 16067043 16070010 16073032 16079016 16080053 16083006 16085056 16087030
16089042 16092001 16065041 16067044 16070012 16073033 16079017 16080054 16083007
16085057 16087031 16089043 16092002 16065042 16068001 16070013 16073034 16079018
16080055 16083008 16085058 16087032 16089044 16092003 16065044 16068003 16070014
16073035 16079019 16081001 16083009 16085061 16087033 16089045 16092015 16065045
16068004 16071016 16073037 16079020 16081002 16083010 16085062 16087042 16089046

16092016 16065046 16068005 16071050 16073038 16079021 16081003 16083011 16085065
16087043 16089047 16092017 16065047 16068006 16071051 16073039 16079022 16081012
16083012 16085067 16087044 16089048 16092018 16065048 16068007 16071052 16073040
16079023 16081013 16083013 16085069 16087045 16089049 16092019 16065060 16068008
16071053 16073045 16079024 16081015 16083014 16085071 16087046 16089050 16092020
16065061 16068009 16071054 16073046 16079027 16081016 16083015 16085072 16087047
16089051 16092021 16065072 16068010 16071055 16073047 16079028 16081017 16083016
16085073 16087048 16089052 16092022 16066001 16068013 16071056 16073048 16079029
16081018 16083017 16085074 16087049 16089053 16092023 16066002 16068014 16071058
16073049 16079030 16081019 16083018 16086001 16087050 16089054 16092033 16066003
16068015 16071059 16073050 16079031 16081020 16083019 16086002 16087051 16090001
16092034 16066004 16068016 16071060 16077021 16079032 16081021 16083042 16086003
16087052 16090002 16092035 16066005 16068017 16071061 16077027 16079033 16081022
16083043 16086004 16087053 16090003 16092036 16066006 16068018 16071076 16077028
16079034 16081024 16083044 16086005 16087054 16090004 16092037 16066007 16068021
16071077 16077029 16079035 16081025 16083045 16086006 16087055 16090005 16092042
16066008 16068022 16071078 16077030 16079036 16081036 16083046 16086007 16088001
16090015 16092044 16066009 16068023 16071079 16077031 16079046 16081037 16083048
16086008 16088016 16090016 16092048 16066011 16068024 16072001 16077032 16079047
16081048 16083049 16086025 16088017 16090017 16092049 16066012 16068025 16072002
16077033 16079048 16081049 16083050 16086026 16088018 16090018 16092050 16066015
16068028 16072003 16077034 16079049 16081050 16083052 16086027 16088019 16090019
16092051 16066016 16068029 16072006 16077037 16079052 16081052 16083053 16086028
16088020 16090020 16092052 16066017 16068030 16072007 16077038 16079054 16081053
16083055 16086030 16088021 16090021 16092053 16066018 16068032 16072008 16077039
16079057 16081054 16083056 16086031 16088022 16090022 16092054 16066019 16068034
16072009 16077040 16079058 16081055 16083057 16086032 16088023 16090023 16092055
16066020 16068035 16072010 16077041 16079059 16081056 16083058 16086033 16088025
16090024 16092063 16066021 16068036 16072012 16077043 16079060 16081057 16083059
16086034 16088026 16090025 16092064 16066026 16068037 16072013 16077047 16079061
16081058 16083060 16086035 16088027 16090026 16092065 16066027 16068038 16072014
16078002 16079062 16081059 16084004 16086036 16088028 16090027 16092066 16066030
16068039 16072022 16078003 16079063 16081060 16084006 16086037 16088029 16090028
16092067 16066031 16068040 16072023 16078004 16080002 16081061 16084007 16086038
16088030 16090029 16092068 16066032 16068042 16072024 16078005 16080004 16082001
16084008 16086039 16088031 16090030 16092070 16066033 16068056 16072025 16078006
16080005 16082002 16084009 16086040 16088040 16090038 16092071 16066035 16068057
16072026 16078008 16080006 16082012 16084011 16086041 16088041 16090039 16093001
16066047 16068058 16072033 16078009 16080012 16082013 16084012 16086042 16088042
16090041 16093002 16066049 16069001 16072034 16078010 16080013 16082017 16084013
16086051 16088043 16090042 16093003 16066050 16069002 16072035 16078011 16080014
16082018 16084014 16086052 16088044 16090044 16093004 16066051 16069003 16072036
16078013 16080015 16082019 16084015 16086053 16088045 16090045 16093011 16066052
16069004 16072038 16078014 16080020 16082022 16085008 16086054 16088046 16090046
16093012 16066053 16069005 16072039 16078028 16080021 16082023 16085009 16087001
16088047 16090047 16093013 16066054 16069006 16072040 16078029 16080022 16082025
16085011 16087002 16088048 16090048 16093014 16066055 16069007 16072041 16078030
16080023 16082027 16085012 16087003 16088049 16090049 16093015 16066059 16069009

16072042 16078031 16080024 16082028 16085013 16087004 16088050 16090050 16093016
16066060 16069010 16072043 16078032 16080025 16082029 16085014 16087005 16089001
16090051 16093017 16067001 16069011 16072058 16078033 16080026 16082039 16085024
16087006 16089002 16090052 16093018 16067003 16069012 16072059 16078034 16080027
16082040 16085025 16087007 16089003 16090053 16067004 16069016 16072060 16078035
16080028 16082041 16085026 16087008 16089004 16091003 16067005 16069053 16072061
16078036 16080029 16082042 16085027 16087009 16089005 16091004 16067006 16069054
16072062 16078037 16080030 16082043 16085028 16087010 16089016 16091005 16067013
16069055 16073001 16078038 16080031 16082046 16085029 16087011 16089017 16091006
16067014 16069062 16073010 16078039 16080032 16082047 16085030 16087019 16089018
16091007 16067015 16069063 16073012 16078040 16080033 16082048 16085031 16087020
16089019 16091008

16094016 16094019 16094020 16094021 16094022 16094025 16094026 16094027
16094028 16094029 16094030 16094032 16094033 16094034 16094035 16094048
16094049 16094050 16094051 16094052 16094053 16094054 16095006 16095007
16095008 16095019 16095020 16095028 16095029 16095030 16095031 16095032
16095033 16095035 16095038 16095039 16095041 16095042 16095043 16095044
16095045 16095046 16096053 16096054 16096062 16096063 16096064 16096065
16096066 16096067 16096068 16096069 16097001 16097002 16097003 16097004
16097005 16097006 16097007 16097008 16097009 16097011 16097012 16097013
16097015 16097016 16097030 16097031 16097032 16097033 16097035 16097036
16097037 16097038 16097039 16097042 16097044 16097045 16097049 16097050
16097057 16097058 16097059 16097064 16097065 16097066 16098001 16098002
16098003 16098004 16098008 16098009 16098010 16098011 16098027 16099002
16099003 16099004 16099005 16099006 16099007 16099008 16099009 16099010
16099011 16099012 16099013 16099014 16099026 16099027 16099028 16099029
16099030 16099042 16099043 16099046 16099048 16099049 16099050 16099051
16099053 16099054 16099055 16099056 16099057 16099059 16099060 16099061
16100052 16100053 16100054 16100055 16100056 16100069 16100070 16100072
16100073 16100074 16100077 16100078 16100079 16100080 16100081 16100082
16100083 16100084 16100085 16100086 16100088 16101002 16101003 16101012
16101013 16101014 16101016 16101019 16101020 16101034 16101035 16101036
16101037 16101038 16101039 16101040 16101041 16101042 16101043 16101044
16101045 16101046 16101047 16101048 16101057 16101058 16102001 16102002
16102003 16102004 16102005 16102007 16102010 16102012 16102014 16102015
16102016 16102017 16102018 16102019 16102020 16102033 16102034 16102035
16102036 16102038 16102039 16102040 16102041 16102042 16102043 16102044
16102045 16102046 16102047 16102048 16102053 16102054 16102055 16102056
16102058 16102061 16102062 16102063 16102064 16102065 16102066 16103002
16103003 16103005 16103006 16103007 16103008 16103009 16103010 16103011
16103012 16103013 16103014 16103015 16103016 16103017 16103018 16103029
16103031 16103032 16103033 16103034 16103035 16103038 16103039 16103041
16103042 16103043 16103044 16103045 16103046 16103047 16103048 16103051
16103052 16104010 16104011 16104015 16104016 16104017 16104018 16104019
16104020 16104021 16104023 16104025 16104027 16104029 16104031 16104034
16104035 16104044 16104045 16104046 16104047 16104049 16104050 16104051
16104052 16104053 16104054 16104055 16104056 16104057 16104059 16104060

16105038 16105039 16105040 16105041 16105042 16105045 16105046 16106002 16106003 16106004 16106005 16106006 16106007 16106008 16106009 16106016 16106017 16106018 16106019 16106020 16106021 16106045 16106048 16106049 16106050 16106051 16106052 16106053 16106054 16106058 16107007 16107010 16107012 16107013 16107014 16107015 16107016 16107018 16107020 16107021 16107022 16107047 16107052 16107055 16107058 16107060 16107061 16107062 16107063 16108001 16108002 16108003 16108004 16108005 16108010 16108011 16108013 16108017 16108018 16108019 16108020 16108028 16108033 16108035 16108036 16108039 16108044 16108056 16108057 16108058 16109001 16109023 16109025 16109026 16109031 16109032 16109033 16109034 16109035 16109037 16109038 16109049 16109050 16109051 16109052 16109053 16109054 16109056 16109057 16109058 16109059 16109060 16109061 16110001 16110002 16110009 16110010 16110011 16110012 16110013 16110014 16110015 16110016 16110017 16110018 16110019 16110020 16110021 16110035 16110036 16110038 16110039 16110040 16110041 16110042 16111001 16111002 16111005 16111025 16111026 16111027 16111028 16111029 16111030 16111031 16111032 16111033 16111034 16111036 16111037 16111038 16111039 16111040 16111041 16111042 16111043 16111049 16111050 16112001 16112002 16112003 16112004 16112005 16112006 16112007 16112008 16112009 16112010 16112011 16112012 16112013 16113003 16113008 16113010 16113011 16113012 16113014 16113015 16113016 16113017 16113019 16113020 16113021 16113022 16113028 16113029 16113040 16113041 16113042 16113043 16113044 16113045 16113048 16113049 16113050 16113051 16113052 16113053 16113055 16113056 16114002 16114003 16114004 16114005 16114006 16114007 16114008 16114009 16114010 16114011 16114012 16114013 16114014 16114015 16114016 16114017 16114018 16114026 16114027 16114028 16114029 16114030 16114031 16114032 16114033 16114041 16114046 16114047 16114048 16114049 16115001 16115002 16115029 16115030 16115033 16115034 16115036 16115037 16115039 16115040 16115041 16115042 16115044 16115045 16115046 16115047 16115048 16115054 16115055 16115056 16115057 16115058 16115059 16115060 16115061 16115062 16115063 16115064 16115065 16115066 16116001 16116002 16116007 16116008 16116009 16116010 16116011 16116033 16116034 16116035 16116037 16116038 16116039 16116040 16116041 16116042 16116043 16116044 16116045 16116046 16116047 16116053 16116054 16116055 16117001 16117002 16117003 16117004 16117005 16117006 16117007 16117011 16117012 16117014 16117017 16117018

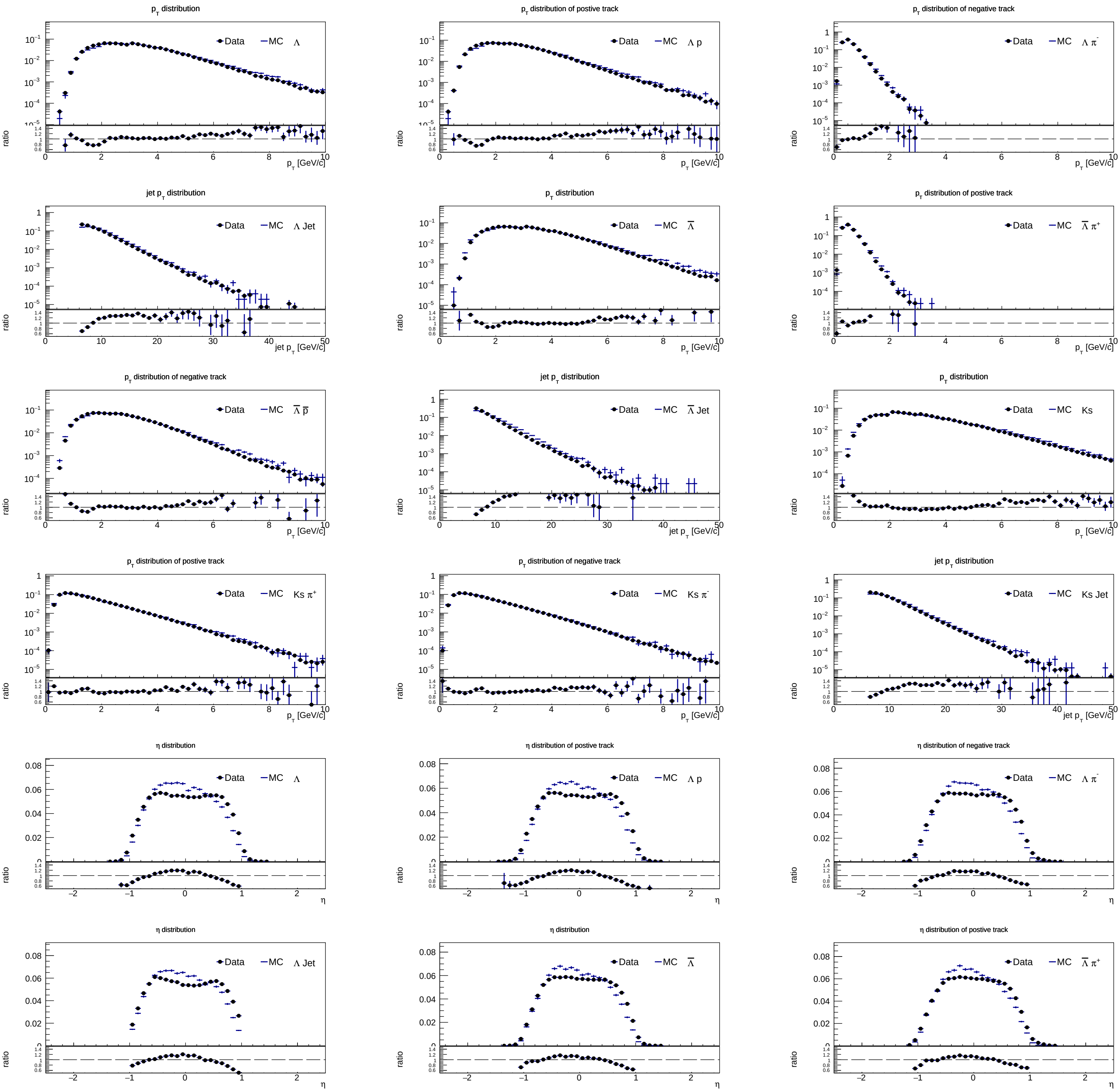
p_T distribution
Data MC Λ
p_T distribution of postive track
Data MC Λ p
p_T distribution of negative track
Data MC Λ π⁻
jet p_T distribution
Data MC Λ Jet
p_T distribution
Data MC Λ̄
p_T distribution of postive track
Data MC Λ̄ π⁺
p_T distribution of negative track
Data MC Λ̄ p̄
jet p_T distribution
Data MC Λ̄ Jet
p_T distribution
Data MC Ks
p_T distribution of postive track
Data MC Ks π⁺
p_T distribution of negative track
Data MC Ks π⁻
jet p_T distribution
Data MC Ks Jet
η distribution
Data MC Λ
η distribution of postive track
Data MC Λ p
η distribution of negative track
Data MC Λ π⁻
η distribution
Data MC Λ Jet
η distribution
Data MC Λ̄
η distribution of postive track
Data MC Λ̄ π⁺
ratio
p_T [GeV/c]
jet p_T [GeV/c]
η

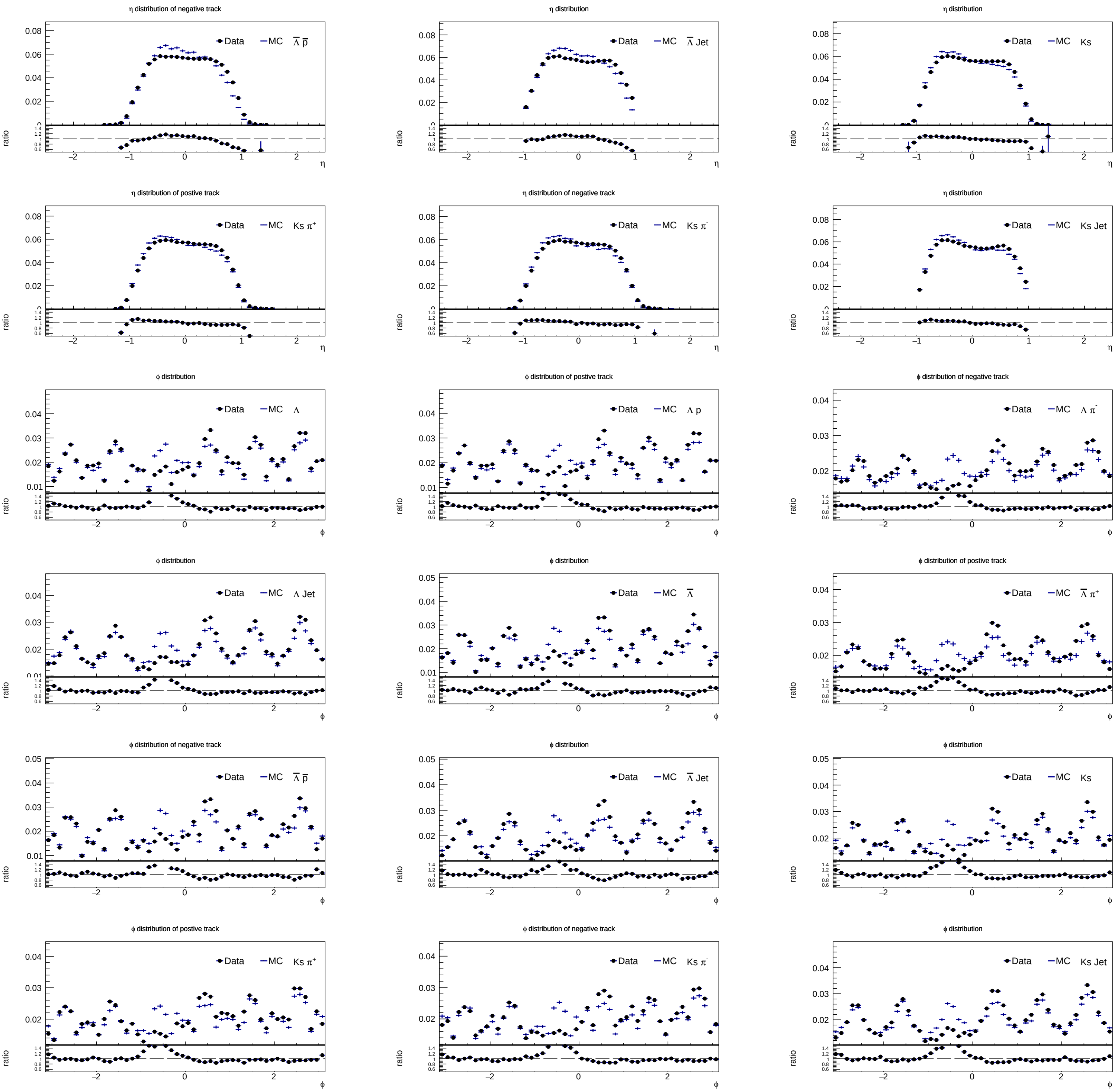
η distribution of negative track
Data MC $\bar{\Lambda}$ $\bar{p}$
η distribution
Data MC $\bar{\Lambda}$ Jet
η distribution
Data MC Ks
η distribution of postive track
Data MC Ks π^+
η distribution of negative track
Data MC Ks π^-
η distribution
Data MC Ks Jet
ϕ distribution
Data MC Λ
ϕ distribution of postive track
Data MC Λ p
ϕ distribution of negative track
Data MC Λ π^-
ϕ distribution
Data MC Λ Jet
ϕ distribution
Data MC $\bar{\Lambda}$
ϕ distribution of postive track
Data MC $\bar{\Lambda}$ π^+
ϕ distribution of negative track
Data MC $\bar{\Lambda}$ $\bar{p}$
ϕ distribution
Data MC $\bar{\Lambda}$ Jet
ϕ distribution
Data MC Ks
ϕ distribution of postive track
Data MC Ks π^+
ϕ distribution of negative track
Data MC Ks π^-
ϕ distribution
Data MC Ks Jet
ratio